

Supporting Information

Hückel Theory + Reorganization Energy = Marcus-Hush Theory — Breakdown of the $1/n$ Trend in π -Conjugated Poly-*p*-phenylene Cation Radicals is Explained

Maxim V. Ivanov, Marat R. Talipov, Anitha Boddada, Sameh H. Abdelwahed,
and Rajendra Rathore*

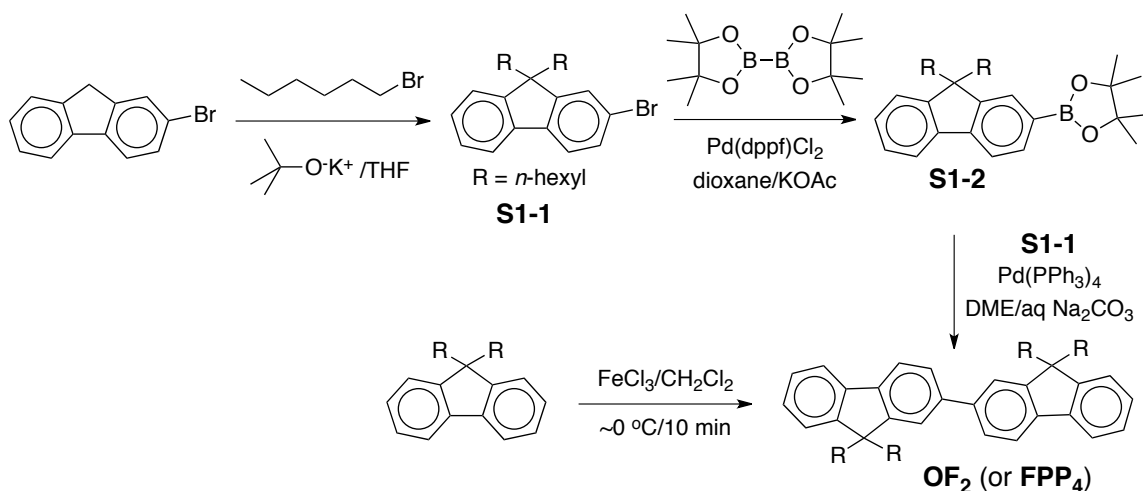
Department of Chemistry, Marquette University, P.O. Box 1881, Milwaukee, WI 53201-1881

Table of Contents

S1. Synthesis of FPP_n	2
S2. Generation of FPP_n^{+•} by redox titrations	24
S3. Density Functional Theory (DFT) calculations	30
Computational details	30
FPP _n in neutral and cation radical states	31
DFT vs experimental results	41
S4. Particle-in-a-box model: comparison of $\cos[\pi/(n+1)]$ and $1/n$ trends	42
S5. Coarse-grained Hückel Molecular Orbital (HMO) theory	43
Parameterization of the coarse-grained HMO model of FPP _n	44
Inclusion of structural reorganization in the HMO theory	47
S6. Multi-State Model (MSM)	49
Application of MSM to FPP _n ^{+•} ,	50
S7. Equilibrium geometrical parameters of FPP_n in neutral and cation radical states	53
S8. References	60

S1. Synthesis of FPP_n

Scheme S1: Synthesis of FPP₄ (OF₂)



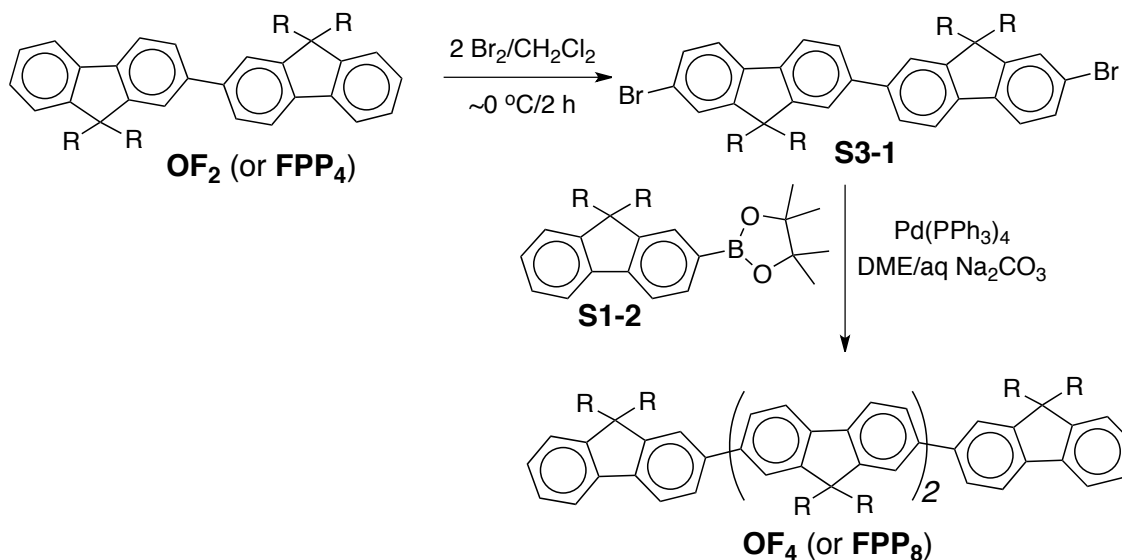
Synthesis of S1-1. A Schlenk flask containing 2-bromofluorene (2.0 g, 8.2 mmol) and THF (20 mL) was cooled to 0 °C; and t-BuOK (2.7 g, 20.4 mmol) was added under an argon atmosphere. The resulting dark red reaction mixture was stirred for 30 minutes and then 1-bromohexane (3.4 g, 20.4 mmol) was added dropwise. The reaction mixture was allowed to warm to room temperature and was stirred for additional 12 hours. The reaction was quenched by an addition of 5% HCl (50 mL) and it was extracted with CH₂Cl₂ (3 x 25 mL). The combined organic layers were washed with water, saturated brine, and dried over anhydrous MgSO₄. It was filtered and evaporated to afford crude product as an oil, which was purified by column chromatography using silica gel and hexanes as eluent (colorless oil, 3.2 g, 94%). ¹H NMR (CDCl₃) δ: 0.50-0.65 (4H, m), 0.71-0.80 (6H, t, *J* = 7.24 Hz), 0.96-1.17 (12H, m), 1.85-2.00 (4H, m), 7.29-7.34 (3H, m), 7.42-7.46 (2H, m), 7.52-7.57 (1H, dd, *J* = 8.75 Hz), 7.63-7.68 (1H, m). ¹³C NMR (CDCl₃) δ: 14.17, 22.74, 23.81, 29.81, 31.63, 40.46, 55.50, 119.88, 121.13, 121.15, 122.98, 126.25, 127.06, 127.60, 130.02, 140.16, 140.27, 150.42, 153.09.

Synthesis of S1-2. To a Schlenk flask containing a degassed solution of KOAc (1.8 g, 18.12 mmol) in dioxane (50 mL) were added S1-1 (2.3 g, 5.6 mmol) and Pd(dppf)Cl₂ (60 mg) under an argon atmosphere. The mixture was stirred for 10 min and then bis(pinacolato)diboron (1.7 g, 6.7 mmol) was added. The resulting mixture was refluxed for 12 h. After cooling to room temperature, the reaction mixture was poured into water (100 mL); and extracted with CH₂Cl₂ (3 x 50 mL). The combined organic layers were washed with water and evaporated. The crude product was purified by column chromatography (SiO₂, hexanes) to afford S1-2 as a colorless liquid (1.97 g, 77%). ¹H NMR (CDCl₃, 400 MHz) δ: 0.48-0.65 (4H, m), 0.71-0.78 (6H, t, *J* = 6.94 Hz), 0.94-1.14 (12H, m), 1.36-1.42 (12H, s), 1.89-2.05 (4H, m), 7.29-7.35 (3H, m), 7.67-7.75 (3H, m), 7.78-7.81 (1H, dd, *J* = 7.46 Hz); ¹³C NMR (CDCl₃, 400 MHz) δ: 14.16, 22.72, 23.77, 25.08, 29.82, 31.61, 40.38, 55.20, 83.83, 119.04, 120.22, 123.05, 126.78, 127.62, 128.94, 133.82, 141.03, 144.26, 149.99, 151.42.

Synthesis of S2-2. The S2-1 (4.4 g, 8.90 mmol) was bornylated using PdCl₂(dppf) (60 mg), dioxane (50 mL), and KOAc (5.3 g, 54.0 mmol), bis(pinacolato)diboron (5.0 g, 19.7 mmol) using the procedure described above for S1-2. The crude product was purified by column chromatography (SiO₂, hexanes) to afford S2-2 as a white powder (4.3 g, 82%). m.p: 82-84 °C; ¹H NMR (CDCl₃, 400 MHz) δ: 0.45-0.62 (4H, m), 0.68-0.78 (6H, t, *J* = 6.86 Hz), 0.92-1.13 (12H, m), 1.34-1.43 (24H, s), 1.93-2.05 (4H, m), 7.69-7.74 (2H, d, *J* = 7.61 Hz), 7.74-7.76 (2H, s), 7.78-7.83 (2H, dd, *J* = 7.55 Hz); ¹³C NMR (CDCl₃, 400 MHz) δ: 14.16, 22.70, 23.68, 25.06, 25.16, 29.75, 31.56, 40.22, 55.29, 83.83, 119.51, 129.03, 133.79, 144.04, 150.57.

Synthesis of OF₃. The monobromide S1-1 (1.73 g, 5.17 mmol) and bis(boronic) ester S2-2 (1.02 g, 2.07 mmol) were subjected to Suzuki coupling in degassed 1,2-dimethoxyethane (60 mL) containing a solution of sodium carbonate (5.0 g) in water (20 mL) and Pd(PPh₃)₄ (90 mg) as a catalyst using the procedure described above for OF₂. Crude product was then purified by column chromatography (silica, hexanes) to afford pure OF₃ (0.88 g, 51%). m.p: 92-94 °C; ¹H NMR (CDCl₃, 400 MHz) δ: 0.60-0.87 (30H, m), 0.99-1.20 (38H, m), 1.97-2.16 (12H, m), 7.29-7.42 (6H, m), 7.60-7.70 (8H, m), 7.72-7.77 (2H, d, *J* = 6.94 Hz), 7.77-7.79 (1H, s), 7.79-7.81 (2H, d, *J* = 2.95 Hz); ¹³C NMR (CDCl₃, 400 MHz) δ: 14.18, 22.72, 23.93, 29.81, 29.85, 31.60, 31.60, 40.53, 55.30, 55.45, 119.87, 120.04, 120.09, 121.55, 121.64, 123.06, 126.17, 126.29, 126.93, 127.14, 140.12, 140.46, 140.63, 140.66, 140.94, 151.13, 151.61, 151.92.

Scheme S3: Synthesis of FPP₈ (OF₄)

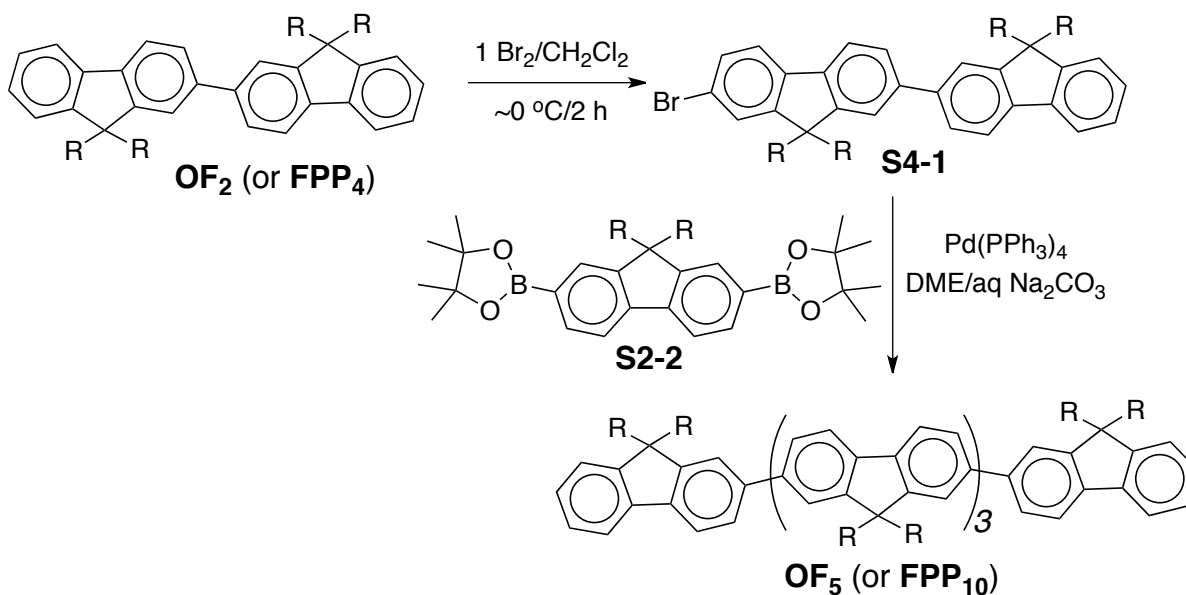


Synthesis of S3-1. A solution of OF₂ (2.8 g, 4.2 mmol) in CH₂Cl₂ (30 mL) under an argon atmosphere was treated dropwise with a solution of Br₂ (1.54 g) in CH₂Cl₂ (10 mL) with the aid of a dropping funnel. After addition was completed (~10 min), the resulting mixture was stirred for additional 2 h at room temperature. The reaction mixture was poured into 5% aqueous NaOH solution (100 mL), CH₂Cl₂ layer was separated and the aqueous layer was extracted with CH₂Cl₂ (3 x 25 mL). The combined organic layers were then washed with water (3 x 25 mL), dried

over anhydrous MgSO₄ and evaporated in vacuo. The crude product was purified by column chromatography (SiO₂, hexanes) to afford pure **S3-1** (1.8 g, 53%). m.p: 108-110 °C; ¹H NMR (CDCl₃, 400 MHz) δ: 0.65-0.75 (8H, m), 0.75-0.82 (12H, t *J* = 6.8 Hz), 1.01-1.20 (24H, m), 1.91-2.10 (8H, m), 7.46-7.50 (4H, m), 7.56-7.65 (6H, m), 7.72-7.76 (2H, d, *J* = 7.89 Hz); ¹³C NMR (CDCl₃, 400 MHz) δ: 14.16, 22.71, 23.86, 29.75, 31.59, 40.41, 55.66, 120.17, 120.99, 121.24, 121.54, 126.35, 126.42, 130.15, 139.48, 139.90, 140.92, 151.27, 153.37.

Synthesis of OF₄. The dibromide **S3-1** (0.1 g, 0.12 mmol) and the boronic ester **S1-2** (0.13 g, 0.28 mmol) were subjected to Suzuki coupling in degassed 1,2-dimethoxyethane (20 mL) containing a solution of sodium carbonate (2.5 g) in water (10 mL) and Pd(PPh₃)₄ (25 mg) as a catalyst using the procedure described above for **OF₂**. Crude product was then purified by column chromatography (silica, hexanes) to afford pure **OF₄** (0.09 g, 55%). m.p: 80-82 °C; ¹H NMR (CDCl₃, 400 MHz) δ: 0.60-0.87 (40H, m), 0.99-1.20 (48H, m), 1.97-2.16 (16H, m), 7.29-7.42 (6H, m), 7.60-7.73 (12H, m), 7.72-7.77 (2H, dd, *J* = 7.11 Hz), 7.77-7.82 (2H, d, *J* = 7.86 Hz), 7.82-7.87 (4H, dd, *J* = 7.83 Hz); ¹³C NMR (CDCl₃, 400 MHz) δ: 14.19, 22.72, 23.93, 23.99, 29.83, 29.86, 31.60, 31.61, 31.64, 40.53, 55.32, 55.47, 119.88, 120.05, 120.12, 121.57, 121.65, 123.07, 126.19, 126.30, 126.95, 127.15, 140.13, 140.17, 140.48, 140.63, 140.69, 140.94, 151.15, 151.61, 151.94, 151.95.

Scheme S4: Synthesis of FPP₁₀ (OF₅)

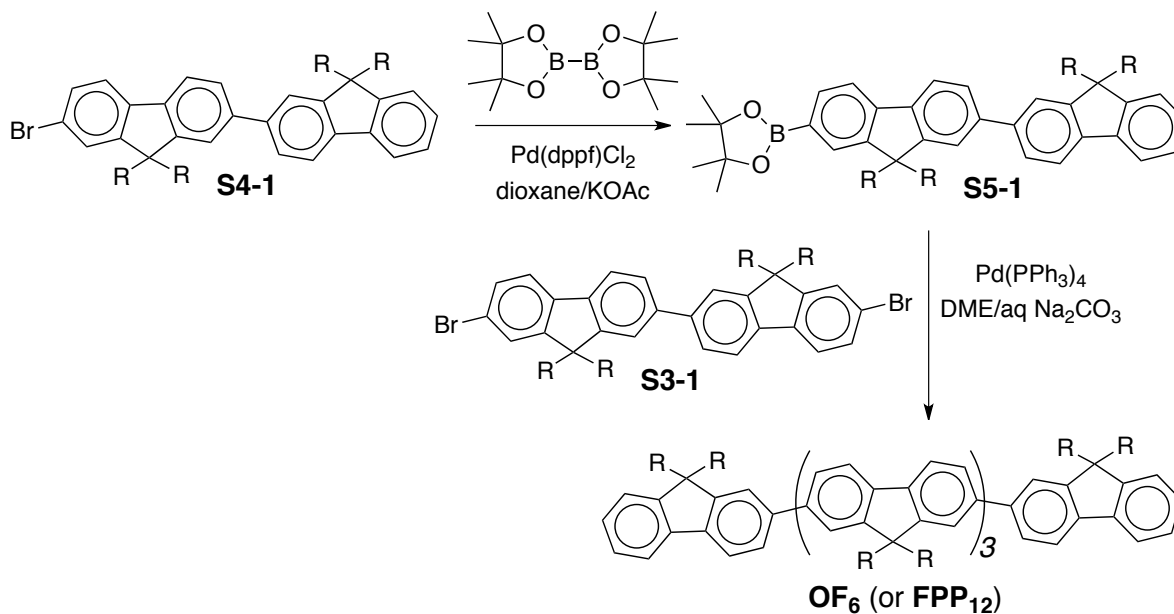


Synthesis of S4-1. A cooled (~0 °C) solution of **OF₂** (2.8 g, 4.2 mmol) and catalytic amount of I₂ (~50 mg) in CH₂Cl₂ (30 mL) was stirred for 5 min under an argon atmosphere and was then treated dropwise with a solution of Br₂ (0.67 g, 4.2 mmol) in CH₂Cl₂ (10 mL) with the aid of a dropping funnel. After addition was completed (~10 min), the resulting mixture was stirred for additional 2 h at ~0 °C. The reaction mixture was poured into 5% aqueous NaOH solution (100 mL), CH₂Cl₂ layer was separated and the aqueous layer was extracted with CH₂Cl₂ (3 x 25 mL). The combined organic layers were then washed with water (3 x 25 mL), dried over anhydrous MgSO₄ and

evaporated in vacuo. The crude product was purified by column chromatography (SiO₂, hexanes) to afford pure **S4-1** (1.2 g, 35%). m.p: 90-92 °C; ¹H NMR (CDCl₃, 400 MHz) δ: 0.60-0.81 (20H, m), 0.98-1.19 (24H, m), 1.90-2.09 (8H, m), 7.28-7.39 (3H, m), 7.44-7.50 (2H, m), 7.55-7.67 (5H, m), 7.70-7.76 (2H, d *J* = 7.65 Hz), 7.76-7.79 (1H, d, *J* = 7.81 Hz); ¹³C NMR (CDCl₃, 400 MHz) δ: 14.19, 22.73, 23.87, 23.90, 23.78, 29.84, 31.61, 31.62, 40.45, 40.52, 55.30, 55.65, 119.90, 120.07, 120.15, 121.13, 121.22, 121.52, 121.53, 123.05, 126.19, 126.32, 126.42, 126.95, 127.20, 130.13, 139.31, 139.97, 140.38, 140.60, 140.84, 141.16, 151.10, 151.21, 151.62, 153.37.

Synthesis of OF₅. The monobromide **S4-1** (1.89 g, 2.53 mmol) and *bis*(boronic) ester **S2-2** (0.5 g, 1.01 mmol) were subjected to Suzuki coupling in degassed 1,2-dimethoxyethane (30 mL) containing a solution of sodium carbonate (2.5 g) in water (10 mL) and Pd(PPh₃)₄ (50 mg) as a catalyst using the procedure described above for **OF₂**. Crude product was then purified by column chromatography (silica, hexanes) to afford pure **OF₅** (0.90 g, 54%). m.p: 88-90 °C; ¹H NMR (CDCl₃, 400 MHz) δ: 0.60-0.90 (50H, m), 0.99-1.20 (60H, m), 1.97-2.19 (20H, m), 7.29-7.42 (6H, m), 7.60-7.90 (26H, m); ¹³C NMR (CDCl₃, 400 MHz) δ: 14.19, 22.72, 23.93, 23.94, 23.96, 23.97, 24.00, 29.83, 29.86, 31.62, 31.63, 40.53, 55.32, 55.48, 119.88, 120.05, 120.13, 121.58, 121.66, 123.07, 126.19, 126.30, 126.95, 127.15, 140.13, 140.17, 140.48, 140.64, 140.67, 140.69, 140.94, 151.16, 151.62, 151.95.

Scheme S5: Synthesis of FPP₁₂ (OF₆)

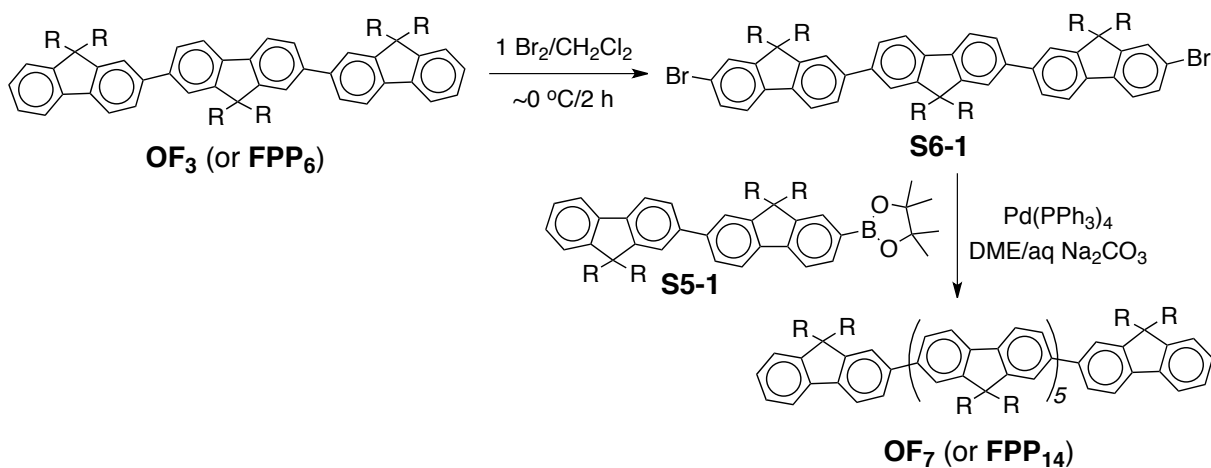


Synthesis of S5-1. The **S4-1** (2.3 g, 3.08 mmol) was bornylated using PdCl₂(dppf) (60 mg), dioxane (50 mL), and KOAc (0.96 g, 9.24 mmol), *bis*(pinacolato)diboron (0.94 g, 3.70 mmol) using the procedure described above for **S1-2**. The crude product was purified by column chromatography (SiO₂, hexanes) to afford **S5-1** as an oil (1.95 g, 80%). ¹H NMR (CDCl₃, 400 MHz) δ: 0.65-0.82 (20H, m), 1.01-1.20 (24H, m), 1.36-1.44 (12H, s), 1.91-2.10 (8H, m), 7.28-7.40 (3H, m), 7.57-7.67 (4H, m), 7.71-7.86 (6H, m); ¹³C NMR (CDCl₃, 400 MHz) δ: 14.16, 22.71, 23.83,

25.09, 29.78, 29.83, 31.58, 31.60, 40.37, 40.51, 55.28, 55.37, 83.84, 119.18, 119.86, 120.01, 120.48, 121.58, 121.63, 123.03, 126.19, 126.92, 127.13, 129.02, 133.96, 140.24, 140.49, 140.90, 141.16, 143.96, 150.32, 151.12, 151.57, 152.19.

Synthesis of OF₆. The dibromide **S3-1** (0.1 g, 0.12 mmol) and the boronic ester **S5-1** (0.22 g, 0.28 mmol) were subjected to Suzuki coupling in degassed 1,2-dimethoxyethane (30 mL) containing a solution of sodium carbonate (2.5 g) in water (10 mL) and Pd(PPh₃)₄ (50 mg) as a catalyst using the procedure described above for **OF₂**. Crude product was then purified by column chromatography (silica, hexanes) to afford pure **OF₆** (0.14 g, 61%). m.p: 82-84 °C; ¹H NMR (CDCl₃, 400 MHz) δ: 0.60-0.90 (60H, m), 0.99-1.20 (72H, m), 1.97-2.19 (24H, m), 7.29-7.42 (6H, m), 7.60-7.90 (32H, m); ¹³C NMR (CDCl₃, 400 MHz) δ: 14.19, 22.72, 23.94, 23.96, 24.00, 29.83, 31.62, 40.53, 55.32, 55.48, 119.88, 120.05, 120.13, 121.58, 121.66, 123.07, 126.95, 127.15, 140.13, 140.17, 140.49, 140.66, 140.68, 140.70, 140.69, 140.94, 151.15, 151.62, 151.96.

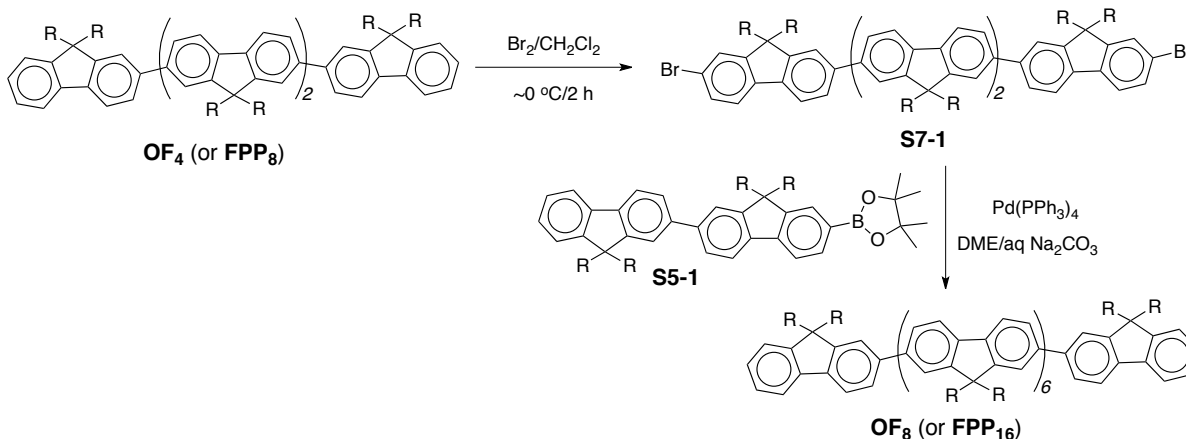
Scheme S6: Synthesis of FPP₁₄ (OF₇)



Synthesis of S6-1. A cooled (~0 °C) solution of **OF₃** (0.3 g, 0.3 mmol) and catalytic amount of I₂ (50 mg) in CH₂Cl₂ (20 mL) under an argon atmosphere was treated dropwise with a solution of Br₂ (0.12 g, 0.75 mmol) in CH₂Cl₂ (10 mL) with the aid of a dropping funnel. After addition was completed (~10 min), the resulting mixture was stirred for additional 2 h at ~0 °C. The reaction mixture was poured into 5% aqueous NaOH solution (100 mL), CH₂Cl₂ layer was separated and the aqueous layer was extracted with CH₂Cl₂ (3 x 25 mL). The combined organic layers were then washed with water (3 x 25 mL), dried over anhydrous MgSO₄ and evaporated in vacuo. The crude product was purified by column chromatography (SiO₂, hexanes) to afford pure **S6-1** (0.25 g, 72%). m.p: 76-78 °C; ¹H NMR (CDCl₃, 400 MHz) δ: 0.65-0.75 (12H, m), 0.75-0.86 (18H, t, *J* = 6.8 Hz), 1.01-1.20 (36H, m), 1.91-2.10 (12H, m), 7.46-7.52 (4H, m), 7.57-7.69 (10H, m), 7.74-7.78 (2H, d, *J* = 7.85 Hz), 7.80-7.85 (2H, d, *J* = 7.85 Hz); ¹³C NMR (CDCl₃, 400 MHz) δ: 14.18, 22.69, 22.72, 23.88, 23.96, 29.77, 31.58, 31.60, 40.44, 55.47, 55.66, 120.17, 121.16, 121.22, 121.55, 121.62, 126.33, 126.42, 130.15, 139.37, 139.96, 140.21, 140.48, 141.12, 151.24, 151.95, 153.37.

Synthesis of OF₇. The dibromide **S6-1** (0.2 g, 0.17 mmol) and the boronic ester **S5-1** (0.31 g, 0.40 mmol) were subjected to Suzuki coupling in degassed 1,2-dimethoxyethane (30 mL) containing a solution of sodium carbonate (2.5 g) in water (10 mL) and Pd(PPh₃)₄ (50 mg) as a catalyst using the procedure described above for **OF₂**. Crude product was then purified by column chromatography (silica, hexanes) to afford pure **OF₇** (0.20 g, 38 %). m.p: 116-118 °C; ¹H NMR (CDCl₃, 400 MHz) δ: 0.60-0.90 (70H, m), 0.99-1.22 (84H, m), 1.97-2.19 (28H, m), 7.29-7.42 (6H, m), 7.60-7.90 (38H, m); ¹³C NMR (CDCl₃, 400 MHz) δ: 14.19, 22.72, 23.94, 24.00, 29.83, 29.86, 31.62, 40.53, 55.32, 55.48, 119.88, 120.05, 120.13, 121.58, 121.66, 123.07, 126.18, 126.31, 126.95, 127.15, 127.37, 140.13, 140.17, 140.49, 140.68, 140.95, 151.15, 151.62, 151.96.

Scheme S7: Synthesis of FPP₁₆ (OF₈)



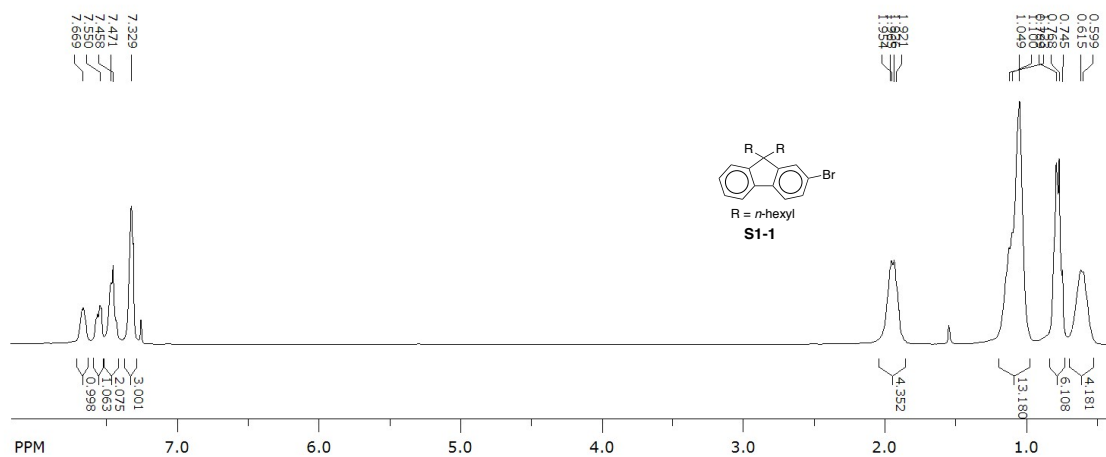
Synthesis of S7-1. A cooled ($\sim 0^\circ\text{C}$) solution of **OF₄** (0.25 g, 0.19 mmol) and catalytic amount of I_2 (50 mg) in CH_2Cl_2 (20 mL) under an argon atmosphere was treated dropwise with a solution of Br_2 (0.08 g, 0.5 mmol) in CH_2Cl_2 (10 mL) with the aid of a dropping funnel. After addition was completed (~ 10 min), the resulting mixture was stirred for additional 2 h at $\sim 0^\circ\text{C}$. The reaction mixture was poured into 5% aqueous NaOH solution (100 mL), CH_2Cl_2 layer was separated and the aqueous layer was extracted with CH_2Cl_2 (3 x 25 mL). The combined organic layers were then washed with water (3 x 25 mL), dried over anhydrous MgSO_4 and evaporated in vacuo. The crude product was purified by column chromatography (SiO_2 , hexanes) to afford pure **S7-1** (0.2 g, 71%). m.p: 84-86 °C; ¹H NMR (CDCl_3 , 400 MHz) δ: 0.65-0.88 (40H, m), 1.01-1.20 (48H, m), 1.91-2.16 (16H, m), 7.46-7.52 (4H, m), 7.57-7.71 (14H, m), 7.74-7.78 (2H, d, $J = 7.85$ Hz), 7.80-7.85 (4H, d, $J = 7.85$ Hz); ¹³C NMR (CDCl_3 , 400 MHz) δ: 14.18, 22.69, 22.72, 23.88, 23.96, 29.77, 29.80, 31.60, 40.44, 40.47, 40.48, 55.47, 55.66, 120.17, 121.13, 121.22, 121.55, 121.62, 121.65, 126.33, 126.42, 130.15, 139.37, 139.96, 140.09, 140.27, 140.42, 140.68, 141.14, 151.24, 151.25, 151.93, 151.96, 153.38.

Synthesis of OF₈. The dibromide **S7-1** (0.14 g, 0.1 mmol) and the boronic ester **S5-1** (0.20 g, 0.25 mmol) were subjected to Suzuki coupling in degassed 1,2-dimethoxyethane (30 mL) containing a solution of sodium carbonate (2.5 g) in water (10 mL) and Pd(PPh₃)₄ (50 mg) as a catalyst using the procedure described above for **OF₂**. Crude product was then purified by column chromatography (silica, hexanes) to afford pure **OF₈** (0.06 g, 26%). m.p: 115-

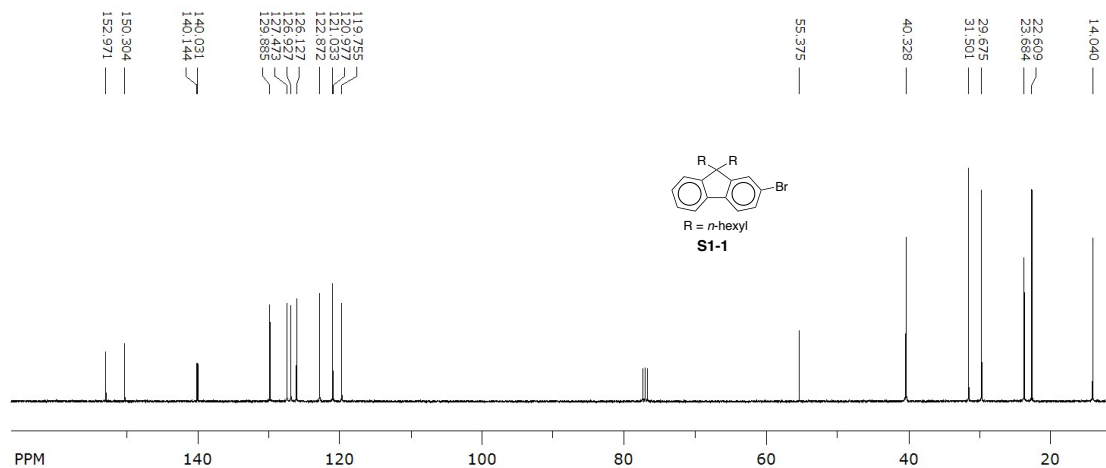
116 °C; ¹H NMR (CDCl₃, 400 MHz) δ: 0.60-0.90 (80H, m), 0.99-1.22 (96H, m), 1.97-2.19 (32H, m), 7.29-7.42 (6H, m), 7.60-7.90 (44H, m); ¹³C NMR (CDCl₃, 400 MHz) δ: 14.19, 22.72, 23.94, 23.99, 24.01, 29.83, 31.62, 40.53, 55.32, 55.48, 119.88, 120.05, 120.15, 121.66, 123.07, 126.18, 126.31, 126.95, 127.19, 140.13, 140.17, 140.49, 140.68, 140.95, 151.15, 151.62, 151.96.

NMR Spectroscopy

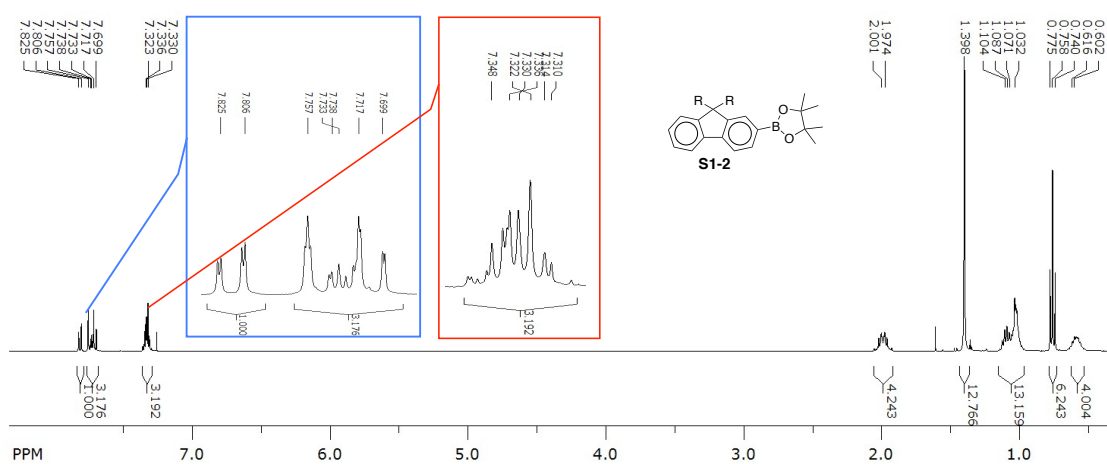
¹H NMR spectrum of S1-1 in CDCl₃



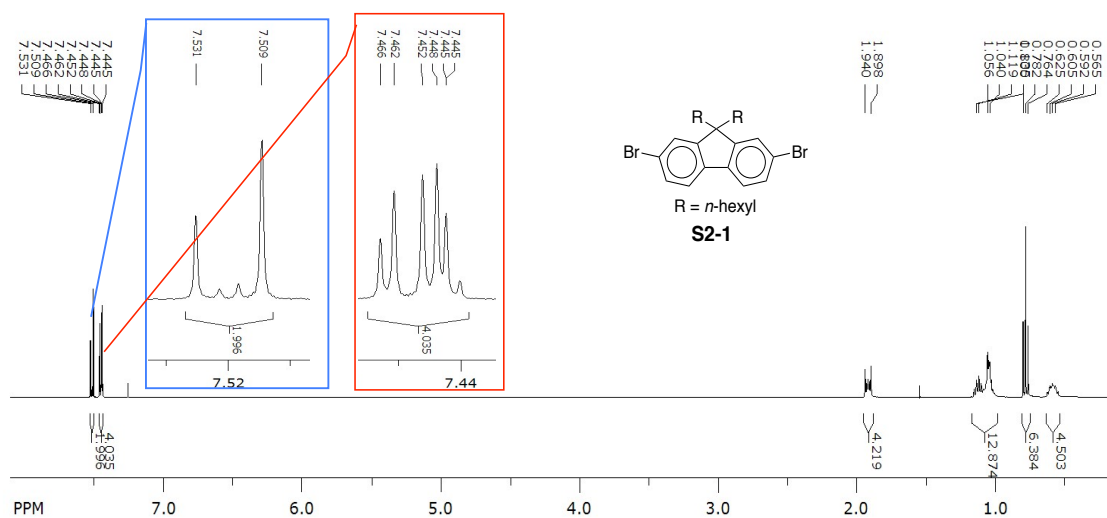
¹³C NMR spectrum of S1-1 in CDCl₃



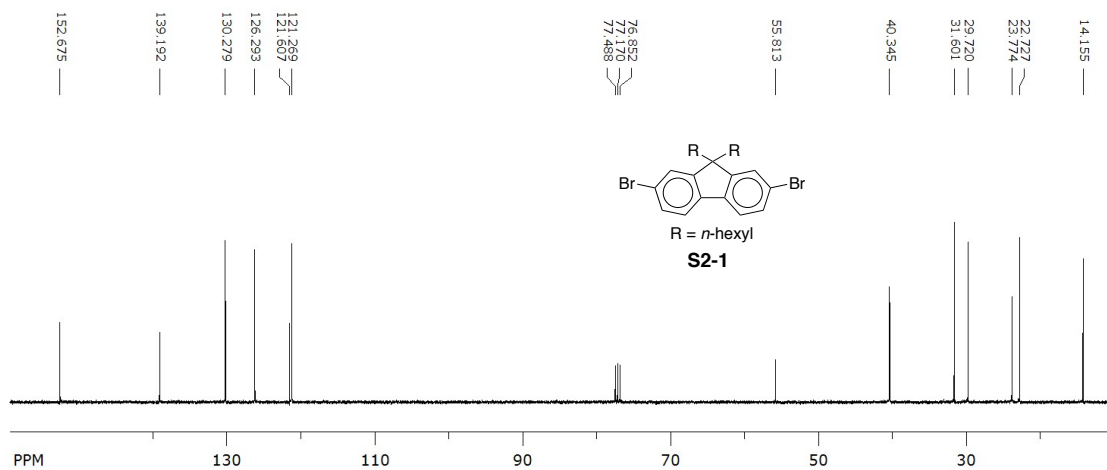
¹H NMR spectrum of S1-2 in CDCl₃



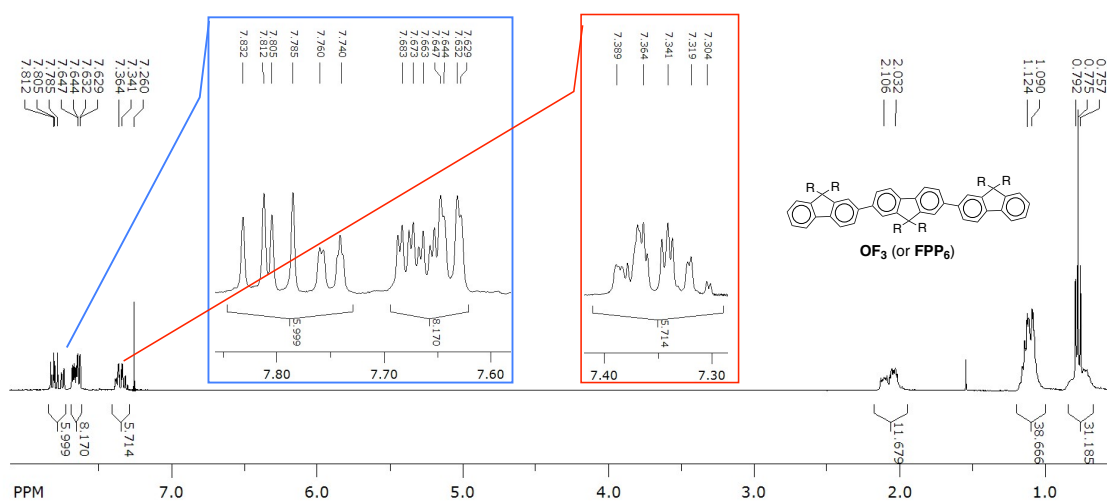
¹H NMR spectrum of S2-1 in CDCl₃



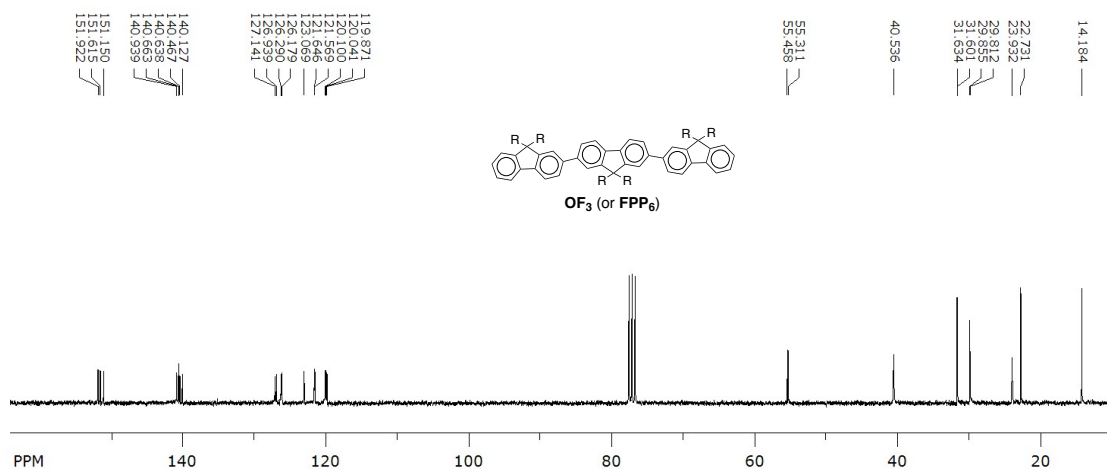
¹³C NMR spectrum of S2-1 in CDCl₃



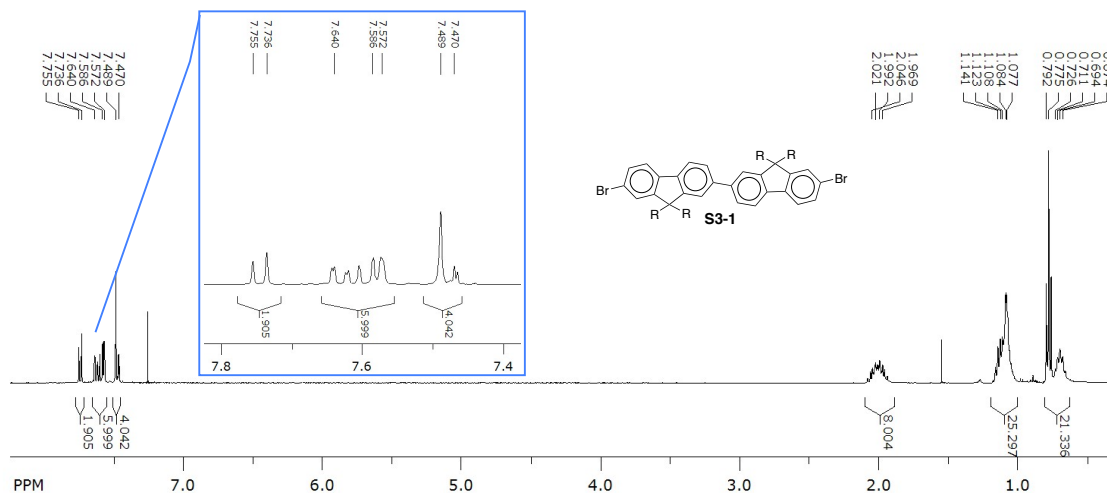
¹H NMR spectrum of OF₃ (or FPP₆) in CDCl₃



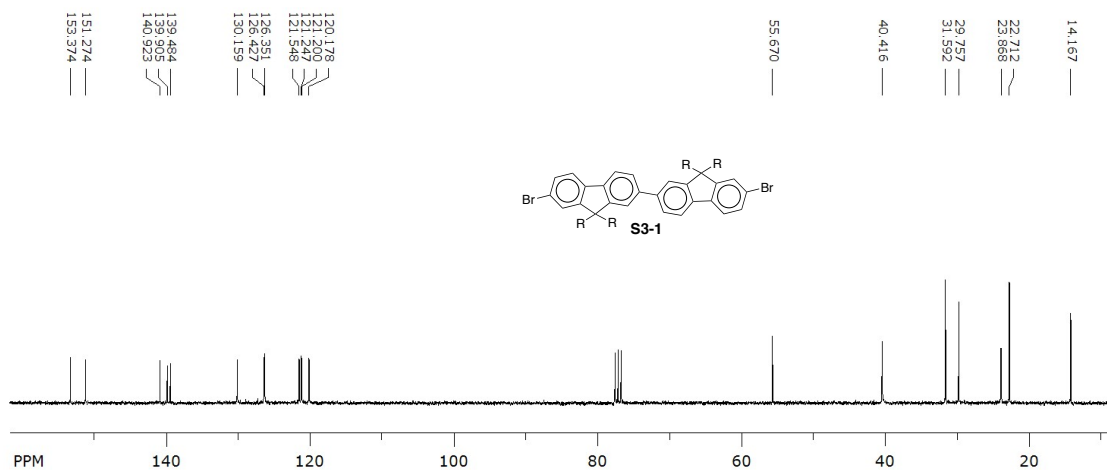
¹³C NMR spectrum of OF₃ (or FPP₆) in CDCl₃



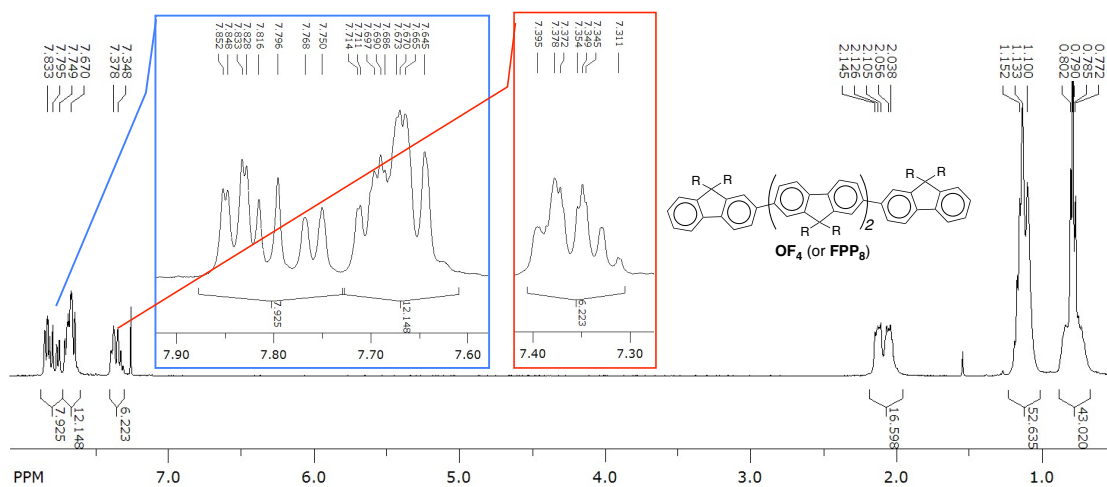
¹H NMR spectrum of S3-1 in CDCl₃



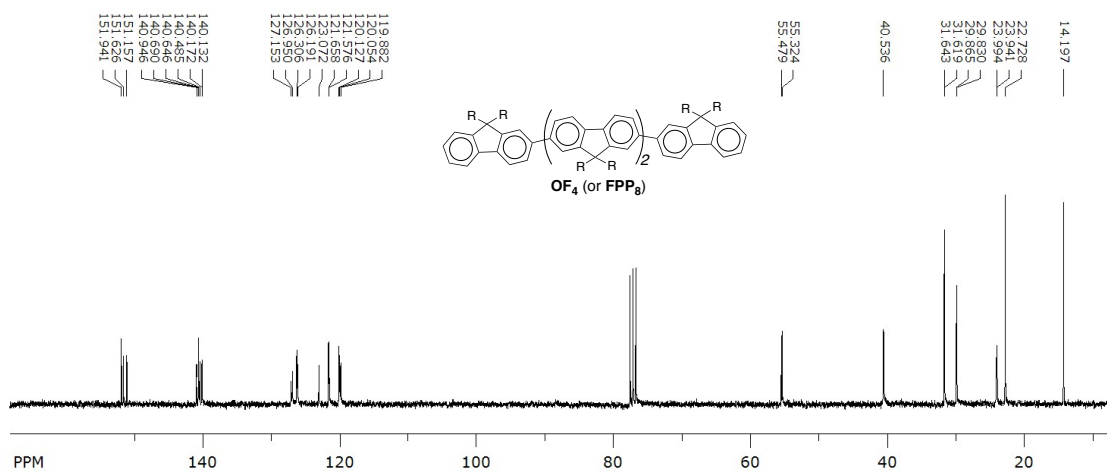
¹³C NMR spectrum of S3-1 in CDCl₃



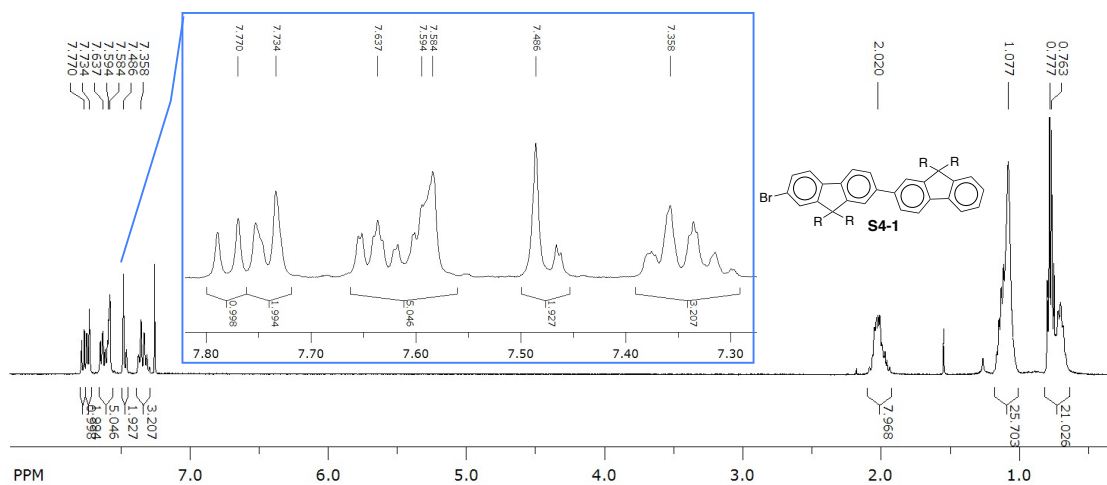
¹H NMR spectrum of OF₄ (or FPP₈) in CDCl₃



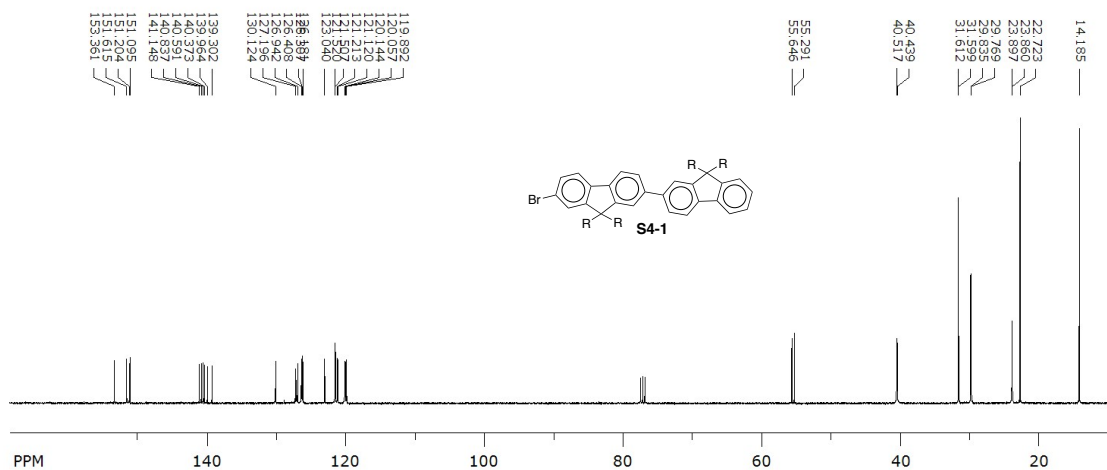
¹³C NMR spectrum of OF₄ (or FPP₈) in CDCl₃



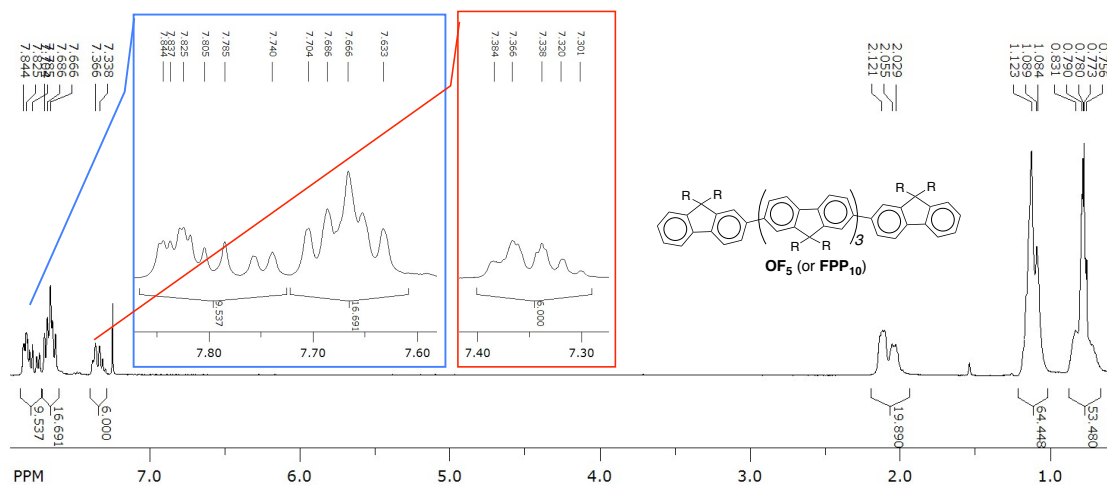
¹H NMR spectrum of S4-1 in CDCl₃



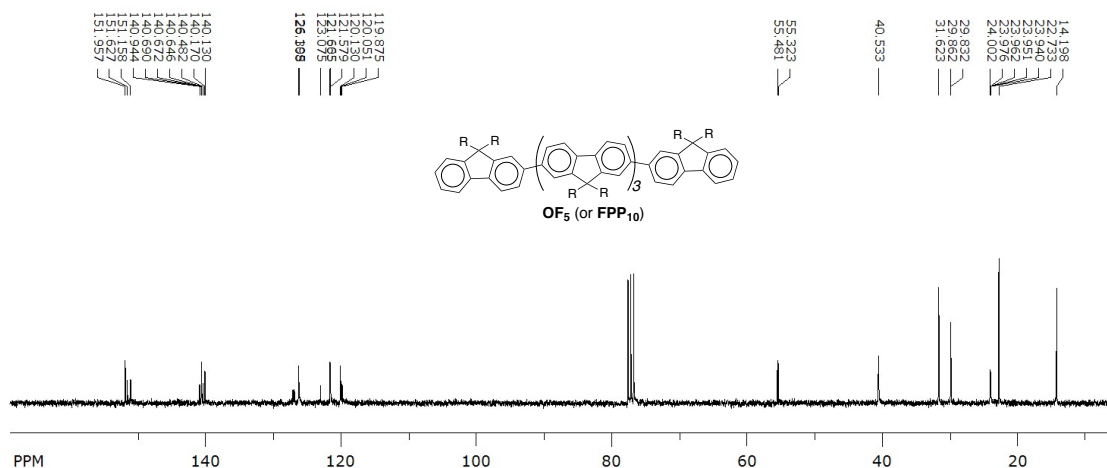
¹³C NMR spectrum of S4-1 in CDCl₃



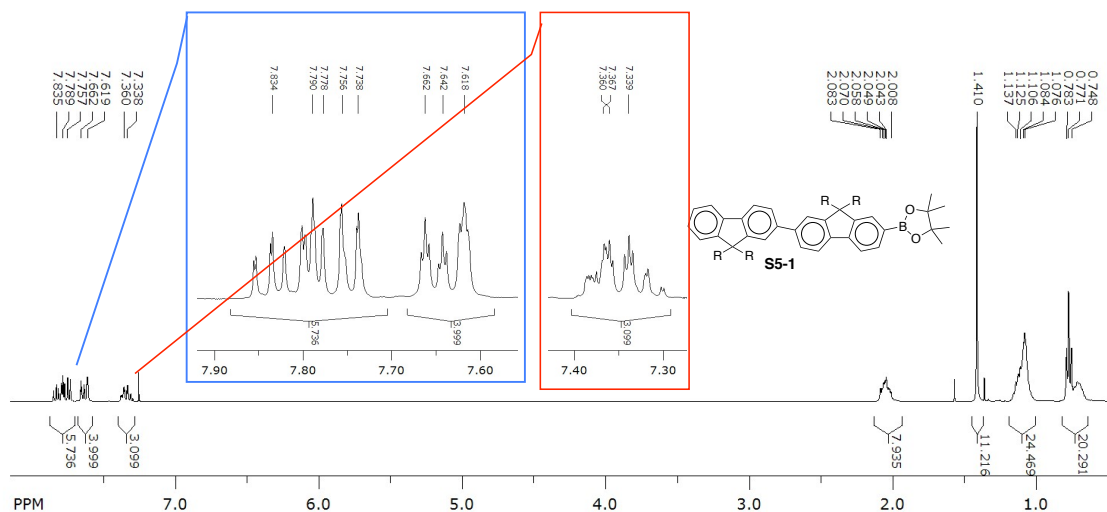
¹H NMR spectrum of OF₅ (or FPP₁₀) in CDCl₃



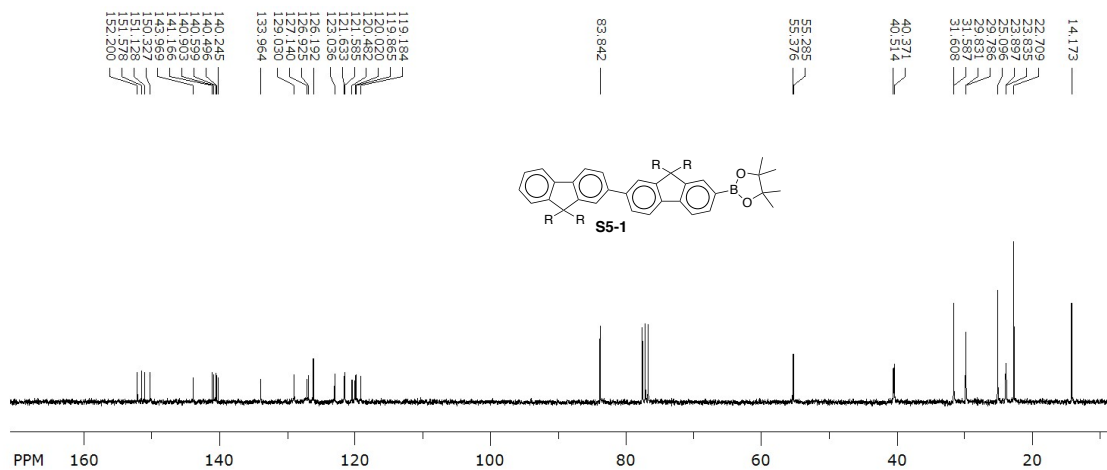
¹³C NMR spectrum of OF₅ (or FPP₁₀) in CDCl₃



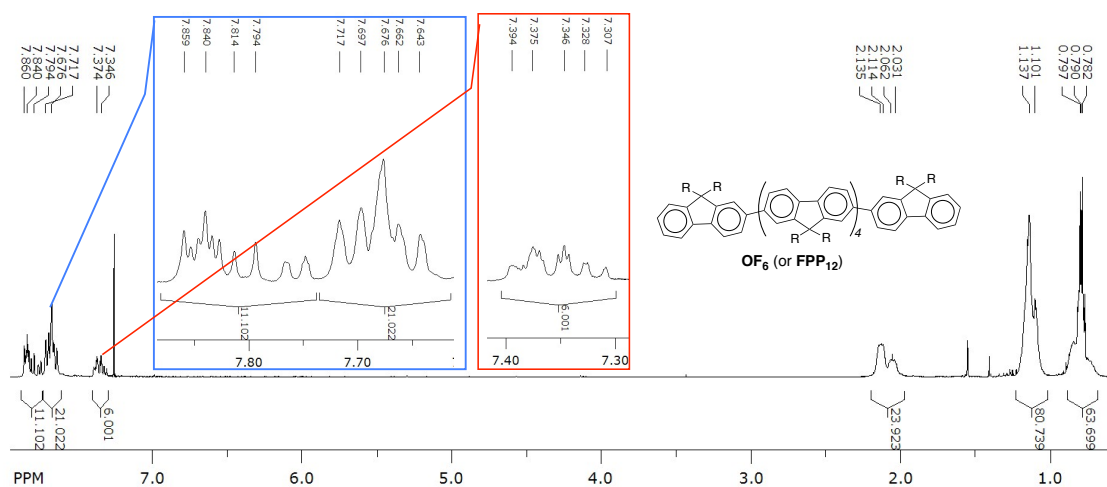
¹H NMR spectrum of S5-1 in CDCl₃



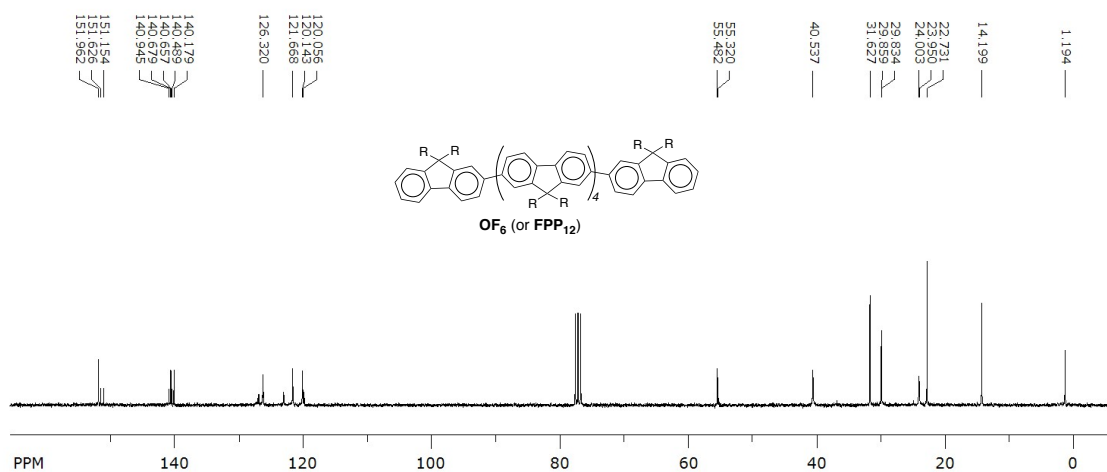
¹³C NMR spectrum of S5-1 in CDCl₃



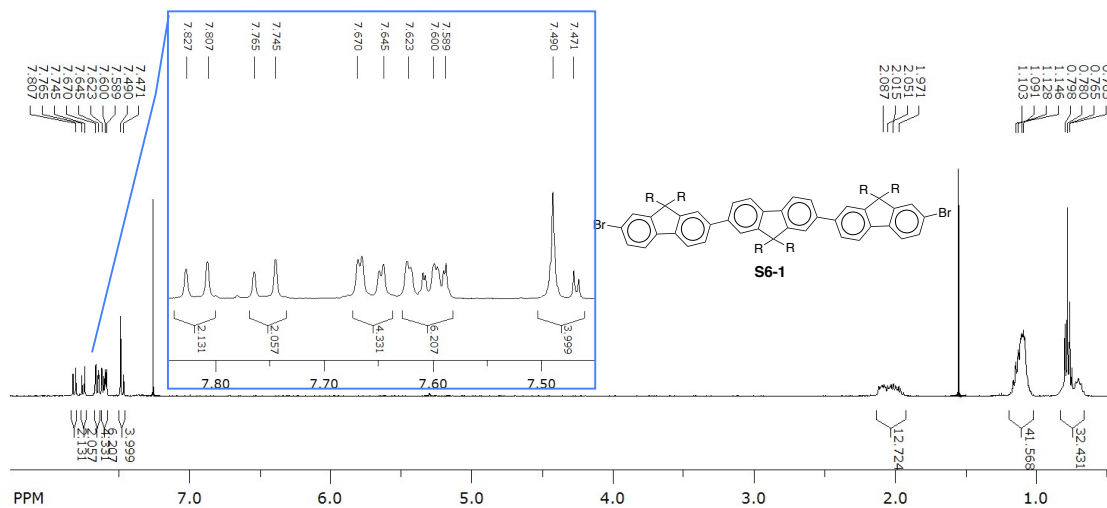
¹H NMR spectrum of OF₆ (or FPP₁₂) in CDCl₃



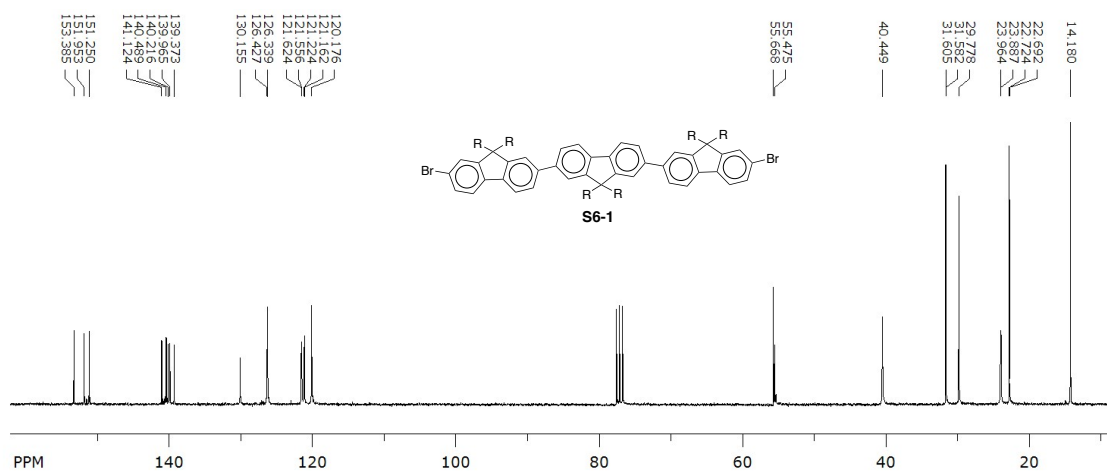
¹³C NMR spectrum of OF₆ (or FPP₁₂) in CDCl₃



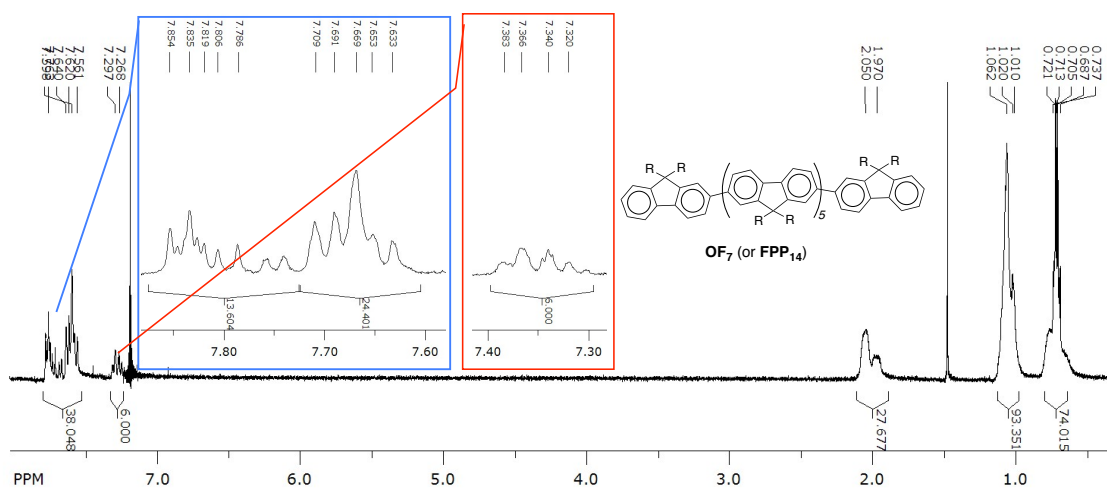
¹H NMR spectrum of S6-1 in CDCl₃



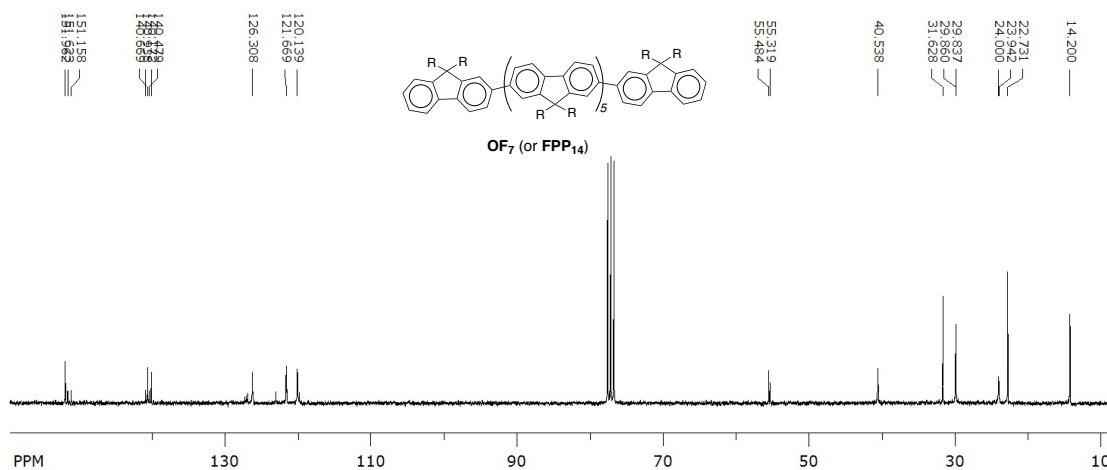
¹³C NMR spectrum of S6-1 in CDCl₃



¹H NMR spectrum of OF₇ (or FPP₁₄) in CDCl₃



¹³C NMR spectrum of OF₇ (or FPP₁₄) in CDCl₃



X-ray crystallography

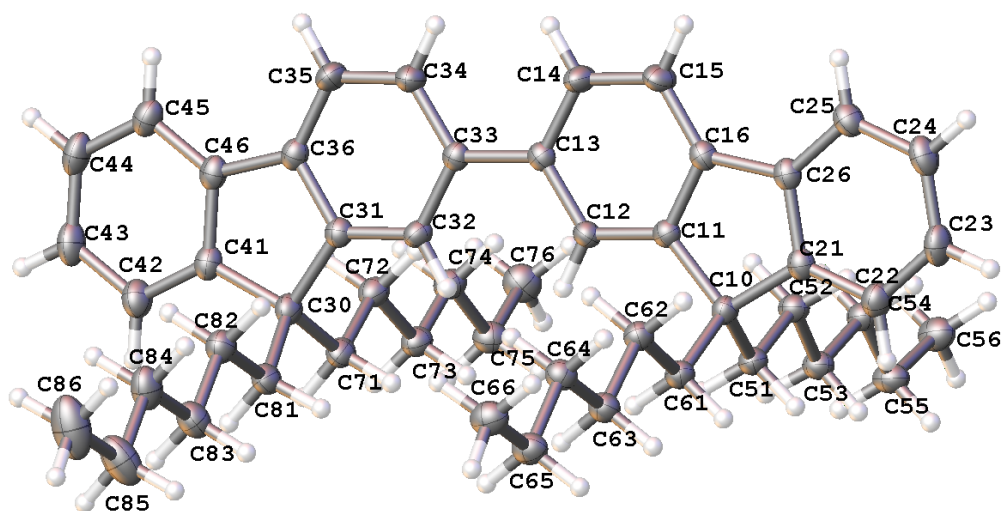


Figure S1. Thermal ellipsoid plots (50% probability) derived from the X-ray crystal structures of **FPP₄**.

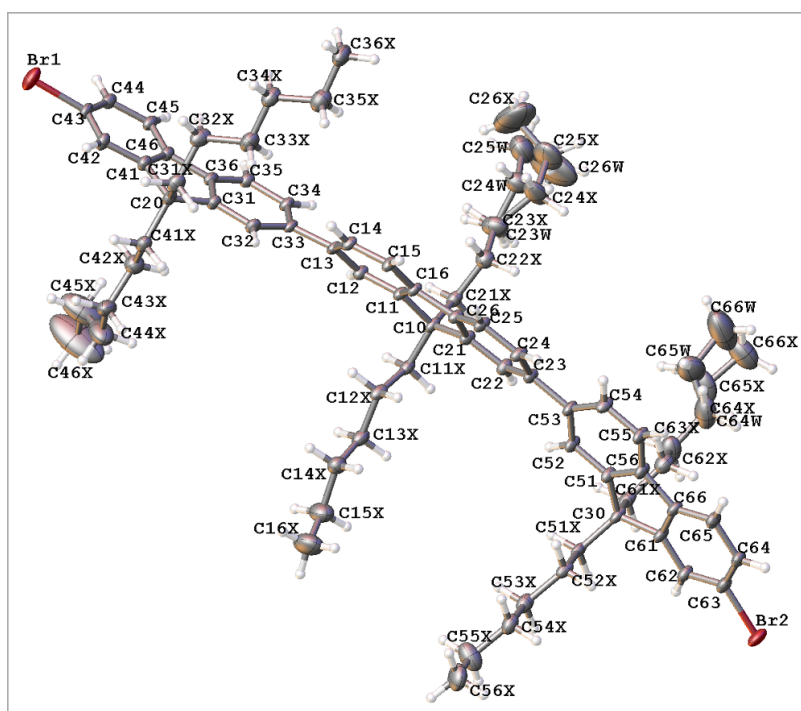


Figure S2. Thermal ellipsoid plots (50% probability) derived from the X-ray crystal structures of **S6-1**.

Table S1. Summary of X-ray crystallographic data collection and structure refinement for **FPP₄** and **S6-1**.

Identification code	raj24w	raj24o
Empirical formula	C ₅₀ H ₆₆	C _{76.95} H _{99.89} Br ₂ Cl _{4.17}
Formula weight	667.03	1332.34
Temperature/K	100.00(10)	100.00(10)

Crystal system	monoclinic	monoclinic
Space group	P2 ₁ /n	P2 ₁ /c
a/Å	15.87557(15)	20.7077(2)
b/Å	15.63800(15)	23.4686(2)
c/Å	16.84324(13)	31.3951(4)
α/°	90.00	90.00
β/°	99.7843(8)	108.9208(12)
γ/°	90.00	90.00
Volume/Å ³	4120.72(6)	14433.0(3)
Z	4	8
ρ _{calc} /cm ³	1.075	1.226
μ/mm ⁻¹	0.441	3.136
F(000)	1464.0	5619.0
Crystal size/mm ³	0.22 × 0.12 × 0.11	0.3989 × 0.3238 × 0.0373
Radiation	CuKα (λ = 1.54184)	CuKα (λ = 1.54184)
2θ range for data collection/°	7.08 to 147.48	6.2 to 147.34°
Index ranges	-16 ≤ h ≤ 19, -18 ≤ k ≤ 19, -20 ≤ l ≤ 20	-25 ≤ h ≤ 21, -29 ≤ k ≤ 27, -38 ≤ l ≤ 38
Reflections collected	40089	100398
Independent reflections	8232 [R _{int} = 0.0272, R _{sigma} = 0.0181]	28598 [R _{int} = 0.0420, R _{sigma} = 0.0343]
Data/restraints/parameters	8232/0/456	28598/7/1566
Goodness-of-fit on F ²	1.032	1.060
Final R indexes [I ≥ 2σ (I)]	R ₁ = 0.0373, wR ₂ = 0.0940	R ₁ = 0.0820, wR ₂ = 0.2159
Final R indexes [all data]	R ₁ = 0.0444, wR ₂ = 0.1002	R ₁ = 0.0980, wR ₂ = 0.2310
Largest diff. peak/hole / e Å ⁻³	0.25/-0.24	1.68/-1.34

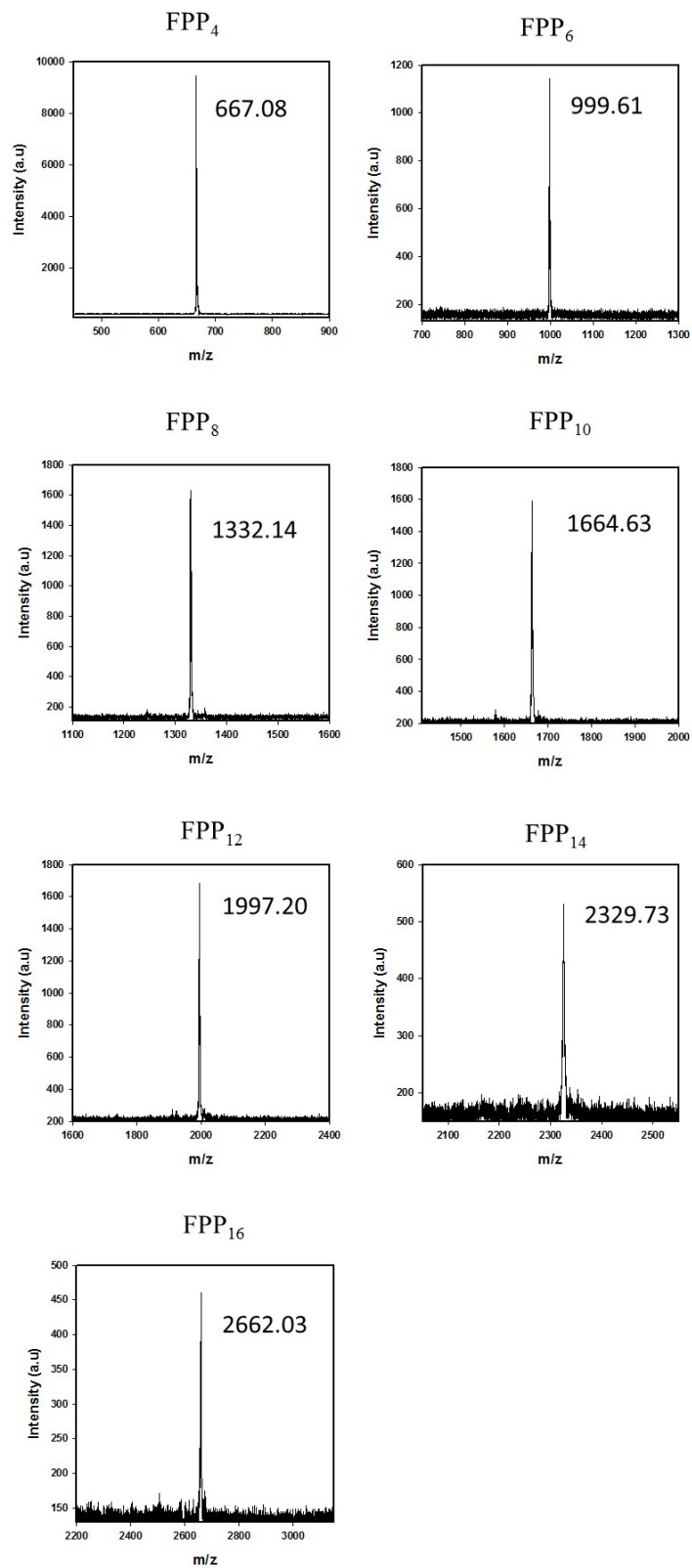


Figure S3. MALDI mass spectroscopy of FPP_n.

Electrochemistry

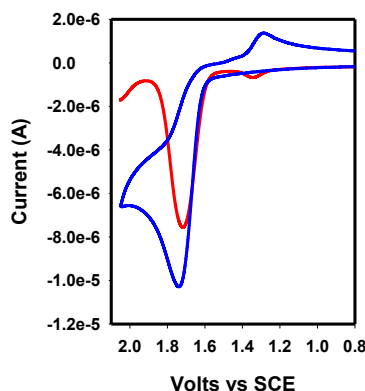


Figure S4. Cyclic voltammogram of OF_1 in CH_2Cl_2 at 22 °C. Note that OF_1 undergoes irreversible electrochemical oxidation due to a facile coupling of OF_1 cation radical with neutral OF_1 to form OF_2 , whose redox peaks can be seen on the return scan.¹

A plot of the first oxidation potentials $E_{\text{ox}1}$ of FPP_n against $\cos(\pi/(n+1))$ showed a linear decrease up to 8 *p*-phenylene units followed by an abrupt breakdown from linearity, i.e. $E_{\text{ox}1}$ remained almost unchanged going from FPP_{10} to FPP_{16} (Table S1). It is noted that evolution of the second and higher oxidation potentials of FPP_n with increasing *n* show drastically varied slopes in E_{ox} vs $\cos(\pi/(n+1))$ plots as compared to $E_{\text{ox}1}$ (Figure S5), suggesting that stabilization of polycations (i.e. dications and trications) is much more effective as compared to cation radicals with increasing *n*. It is interesting to note that the first, second and third oxidation potentials are converging to a single potential. A detailed experimental and computational investigation is planned to explore the role of multiplicity, i.e. singlet vs triplet dications and doublet vs quintet trications, and their respective stabilities in comparison to doublet cation radicals.

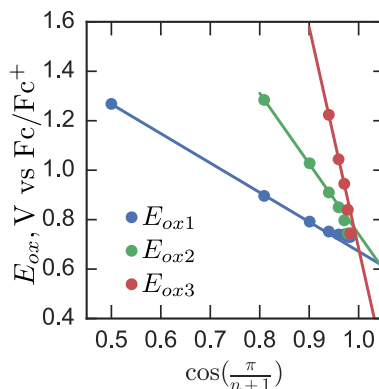


Figure S5. Experimental first, second and third oxidation potentials E_{ox} of FPP_n against $\cos(\pi/(n+1))$.

Table S2. First, second and third oxidation potentials of FPP_n in V vs Fc/Fc^+ .

<i>n</i>	2	4	6	8	10	12	14	16
$E_{\text{ox}1}$	1.27	0.90	0.79	0.75	0.74	0.74	0.73	0.73
$E_{\text{ox}2}$		1.28	1.03	0.91	0.85	0.80	0.73	0.73
$E_{\text{ox}3}$				1.22	1.04	0.95	0.84	0.73

S2. Generation of $\text{FPP}_n^{+\bullet}$ by redox titrations

The reproducible spectra of cation radicals of FPP_n in dichloromethane at 22 °C were obtained by quantitative redox titrations using three different aromatic oxidants, i.e. $\text{THEO}^{+\bullet}\text{SbCl}_6^-$ ($E_{\text{red1}} = 0.67$ V vs Fc/Fc^+ , $\lambda_{\text{max}} = 518$ nm, $\epsilon_{\text{max}} = 7300$ $\text{cm}^{-1} \text{M}^{-1}$),² $\text{NAP}^{+\bullet}\text{SbCl}_6^-$ ($E_{\text{red1}} = 0.94$ V vs Fc/Fc^+ , $\lambda_{\text{max}} = 672$ nm, $\epsilon_{\text{max}} = 9300$ $\text{cm}^{-1} \text{M}^{-1}$)³⁻⁵ and $\text{TRUX}^{+\bullet}\text{SbCl}_6^-$ ($E_{\text{red1}} = 0.78$ V vs Fc/Fc^+ , $\lambda_{\text{max}} = 1400$ nm, $\epsilon_{\text{max}} = 9216$ $\text{cm}^{-1} \text{M}^{-1}$).

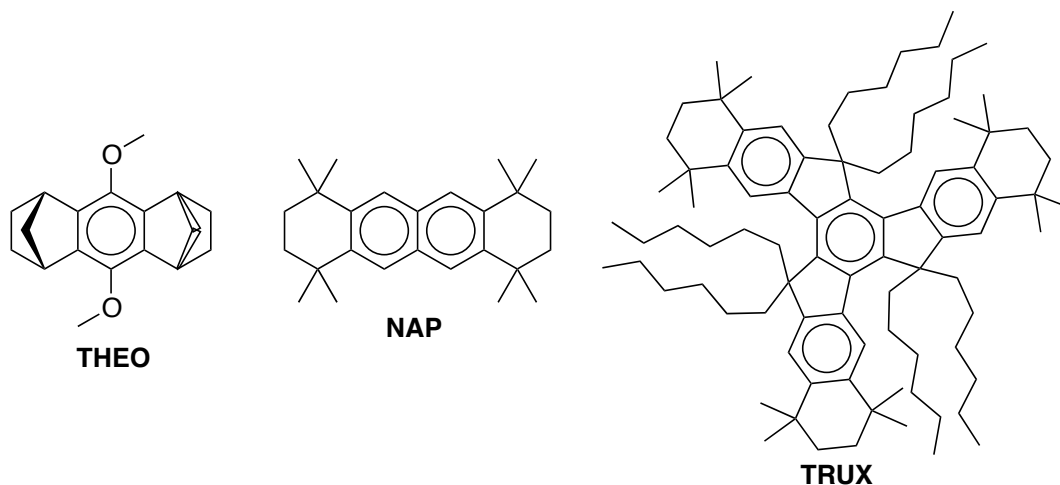
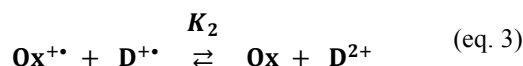
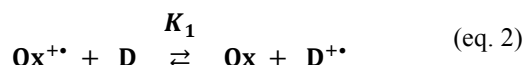


Figure S6. Chemical structures and names of three aromatic oxidants used in redox titrations.

Each redox titration experiment was carried out by an incremental addition of sub-stoichiometric amounts of electron donor (FPP_n) to the solution of an oxidant cation radical ($\text{Ox}^{+\bullet}$). The $1-e^-$ oxidation of FPP_n to $\text{FPP}_n^{+\bullet}$ and reduction of $\text{Ox}^{+\bullet}$ to Ox can be described by an equilibrium shown in eq. 1.



The redox titrations with two successive $1-e^-$ oxidations involve multiple equilibria: one- and two-electron redox reactions between the donor and oxidant (eqs. 2 and 3) and comproportionation/disproportionation of $\text{D}^{2+}/\text{D}^{+\bullet}$ (eq. 4).



Numerical deconvolution^{6,7} of the UV-VIS absorption spectrum at each increment (Figures S7-S19, A) produced the individual spectra of $\text{FPP}_n^{+\bullet}$ and/or FPP_n^{2+} and $\text{Ox}^{+\bullet}$ (Figures S7-S19, B). Moreover, the resulting individual spectra of $\text{Ox}^{+\bullet}$, $\text{FPP}_n^{+\bullet}$, and FPP_n^{2+} provided the mole fractions of each species which were plotted against the added equivalents of FPP_n (Figures S7-S19, C). The mole fraction/equivalent of added donor FPP_n (MF/D) plots were fitted by varying $\Delta G_1 (= E_{\text{ox1}}^{\text{FPP}_n} - E_{\text{red}}^{\text{Ox}^{+\bullet}})$ and $\Delta G_{12} (= E_{\text{ox2}}^{\text{FPP}_n} - E_{\text{ox1}}^{\text{FPP}_n})$.^{6,7}

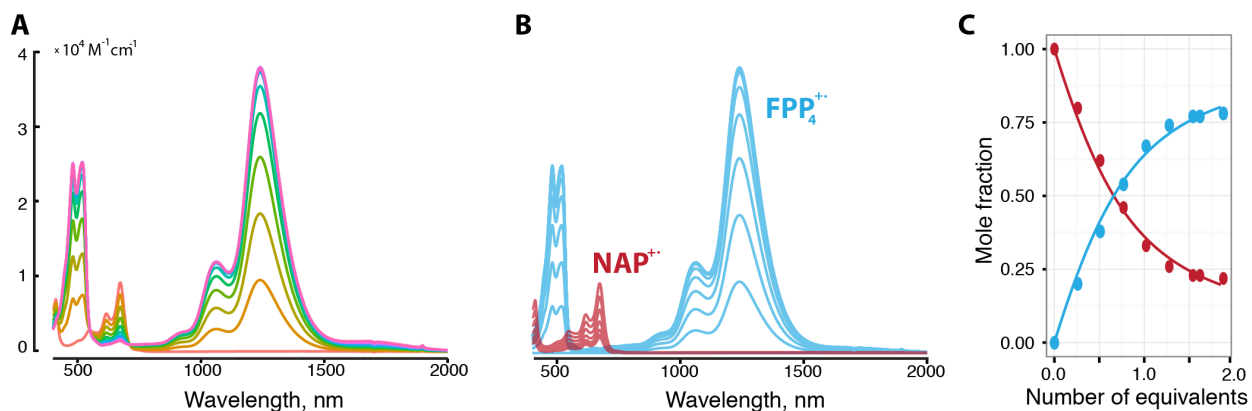


Figure S7. A: Spectral changes observed upon the reduction of 0.061 mM NAP^{++} in CH_2Cl_2 (3 mL) by addition of 15- μL increments of 0.96 mM solution of FPP_4 in CH_2Cl_2 . B: Deconvolution of each UV-VIS absorption spectrum from figure A into its component spectra, i.e. NAP^{++} and FPP_4^{++} (as indicated). C: Plot of the mole fractions of NAP^{++} (red) and FPP_4^{++} (blue) against the added equivalents of FPP_4 . Symbols represent experimental points, while the solid lines show best-fit to the experimental points using $\Delta G_1 = -29 \text{ mV}$.

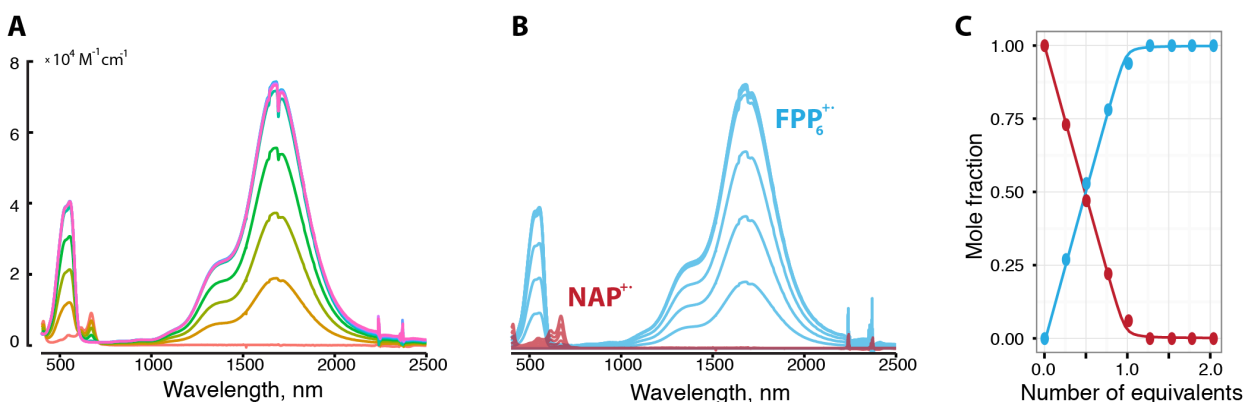


Figure S8. A: Spectral changes observed upon the reduction of 0.038 mM NAP^{++} in CH_2Cl_2 (3 mL) by addition of 30- μL increments of 0.25 mM solution of FPP_6 in CH_2Cl_2 . B: Deconvolution of each UV-VIS absorption spectrum from figure A into its component spectra, i.e. NAP^{++} and FPP_6^{++} (as indicated). C: Plot of the mole fractions of NAP^{++} (red) and FPP_6^{++} (blue) against the added equivalents of FPP_6 . Symbols represent experimental points, while the solid lines show best-fit to experimental points using $\Delta G_1 = -122 \text{ mV}$.

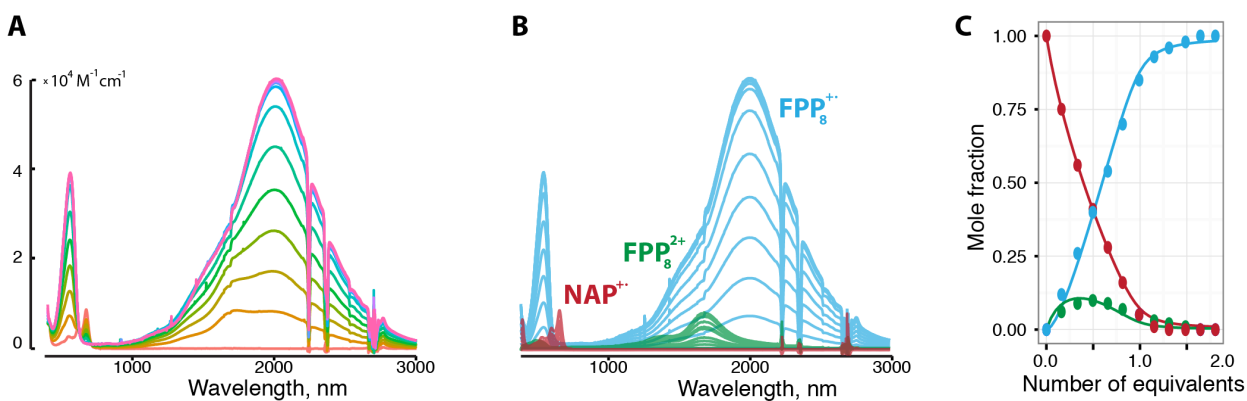


Figure S9. A: Spectral changes observed upon the reduction of 0.06 mM NAP^{++} in CH_2Cl_2 (3 mL) by addition of 14- μL increments of 0.45 mM solution of FPP_8 in CH_2Cl_2 . B: Deconvolution of each UV-VIS absorption spectrum from figure A into

its component spectra, i.e. NAP^{2+} , FPP_8^{2+} and FPP_8^{2+} . **C**: Plot of the mole fractions of NAP^{2+} (red), FPP_8^{2+} (blue) and FPP_8^{2+} (green) against the added equivalents of FPP_8 . Symbols represent experimental points, while the solid lines show best-fit to experimental points using $\Delta G_1 = -123$ mV and $\Delta G_{12} = 149$ mV.

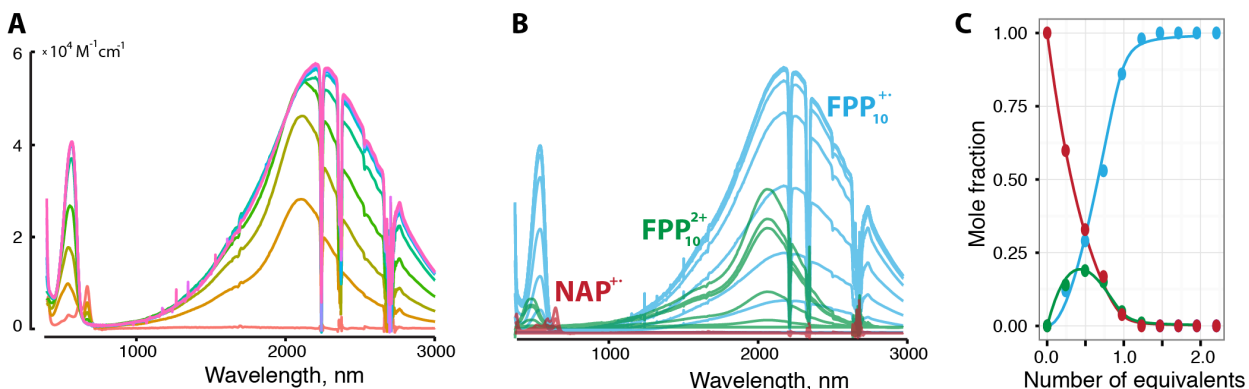


Figure S10. **A**: Spectral changes observed upon the reduction of 0.044 mM NAP^{2+} in CH_2Cl_2 (3 mL) by addition of 15- μL increments of 0.29 mM solution of FPP_{10} in CH_2Cl_2 . **B**: Deconvolution of each UV-VIS absorption spectrum from figure A into its component spectra, i.e. NAP^{2+} , FPP_{10}^{2+} and FPP_{10}^{+} . **C**: Plot of the mole fractions of NAP^{2+} (red), FPP_{10}^{2+} (blue) and FPP_{10}^{+} (green) against the added equivalents of FPP_{10} . Symbols represent experimental points, while the solid lines show best-fit to experimental points using $\Delta G_1 = -152$ mV and $\Delta G_{12} = 144$ mV.

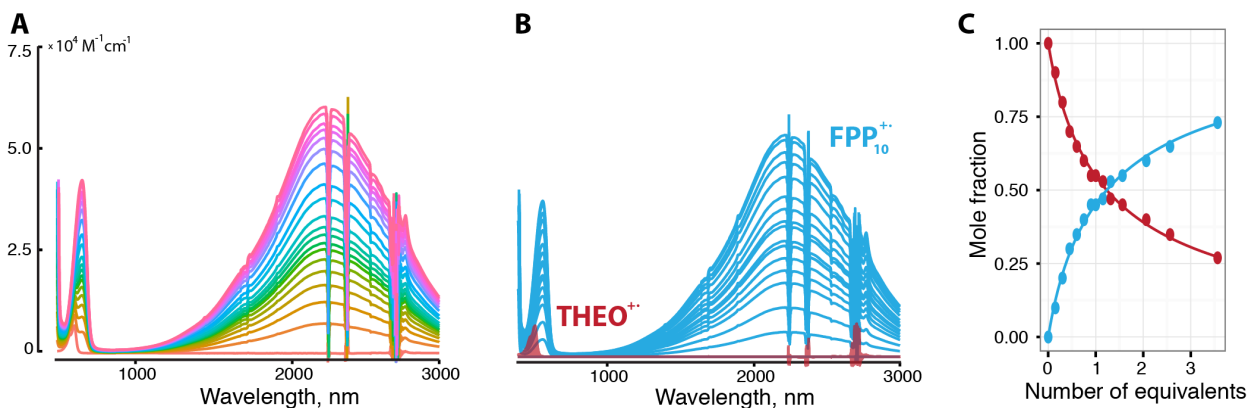


Figure S11. **A**: Spectral changes observed upon the reduction of 0.07 mM THEO^{2+} in CH_2Cl_2 (3 mL) by an addition of 15- μL increments of 0.7 mM solution of FPP_{10} in CH_2Cl_2 . **B**: Deconvolution of each UV-VIS absorption spectrum from figure A into its component spectra, i.e. THEO^{2+} and FPP_{10}^{+} . **C**: Plot of the mole fractions of THEO^{2+} (red) and FPP_{10}^{+} (blue) against the added equivalents of FPP_{10} . Symbols represent experimental points, while the solid lines show best-fit to experimental points using $\Delta G_1 = 10$ mV.

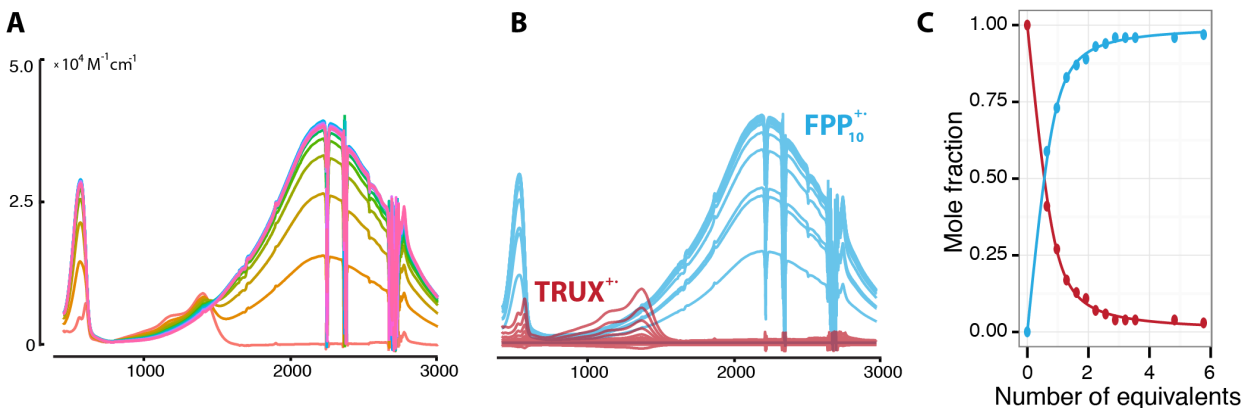


Figure S12. A: Spectral changes observed upon the reduction of 0.019 mM TRUX^{++} in CH_2Cl_2 (3 mL) by addition of 15- μL increments of 0.4 mM solution of FPP_{10} in CH_2Cl_2 . B: Deconvolution of each UV-VIS absorption spectrum from figure A into its component spectra, i.e. TRUX^{++} and FPP_{10}^{++} . C: Plot of the mole fractions of TRUX^{++} (red) and FPP_{10}^{++} (blue) against the added equivalents of FPP_{10} . Symbols represent experimental points, while the solid lines show best-fit to experimental points using $\Delta G_1 = -56 \text{ mV}$.

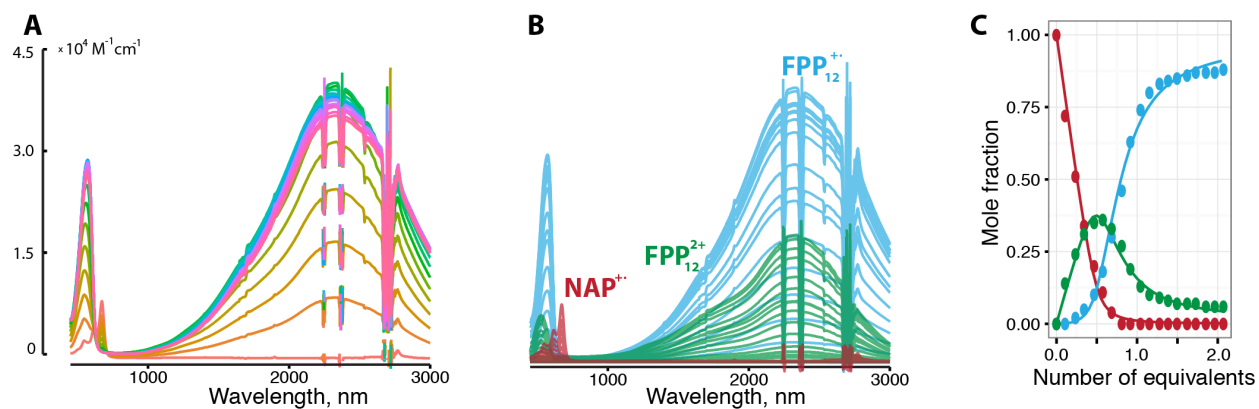


Figure S13. A: Spectral changes observed upon the reduction of 0.123 mM NAP^{++} in CH_2Cl_2 (3 mL) by addition of 10- μL increments of 0.41 mM solution of FPP_{12} in CH_2Cl_2 . B: Deconvolution of each UV-VIS absorption spectrum from figure A into its component spectra, i.e. NAP^{++} , FPP_{12}^{2+} and FPP_{12}^{++} . C: Plot of the mole fractions of NAP^{++} (red), FPP_{12}^{++} (blue) and FPP_{12}^{2+} (green) against the added equivalents of FPP_{12} . Symbols represent experimental points, while the solid lines show best-fit to experimental points using $\Delta G_1 = -155 \text{ mV}$ and $\Delta G_{12} = 144 \text{ mV}$.

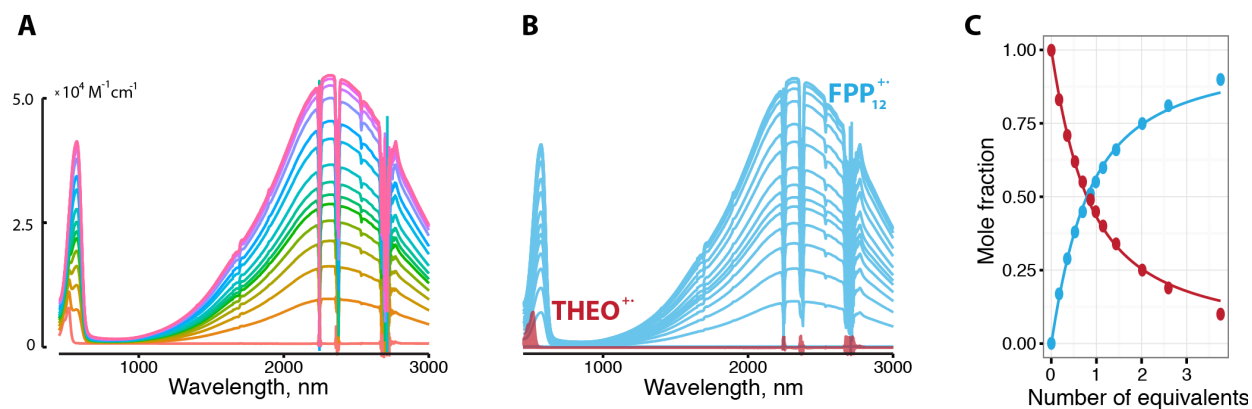


Figure S14. A: Spectral changes observed upon the reduction of 0.058 mM THEO^{++} in CH_2Cl_2 (3 mL) by addition of 15- μL increments of 0.68 mM solution of FPP_{12} in CH_2Cl_2 . B: Deconvolution of each UV-VIS absorption spectrum from figure A into

its component spectra, i.e. THEO^{2+} and FPP_{12}^{2+} . **C**: Plot of the mole fractions of THEO^{2+} (red) and FPP_{12}^{2+} (blue) against the added equivalents of FPP_{12} . Symbols represent experimental points, while the solid lines show best-fit to experimental points using $\Delta G_1 = -14$ mV.

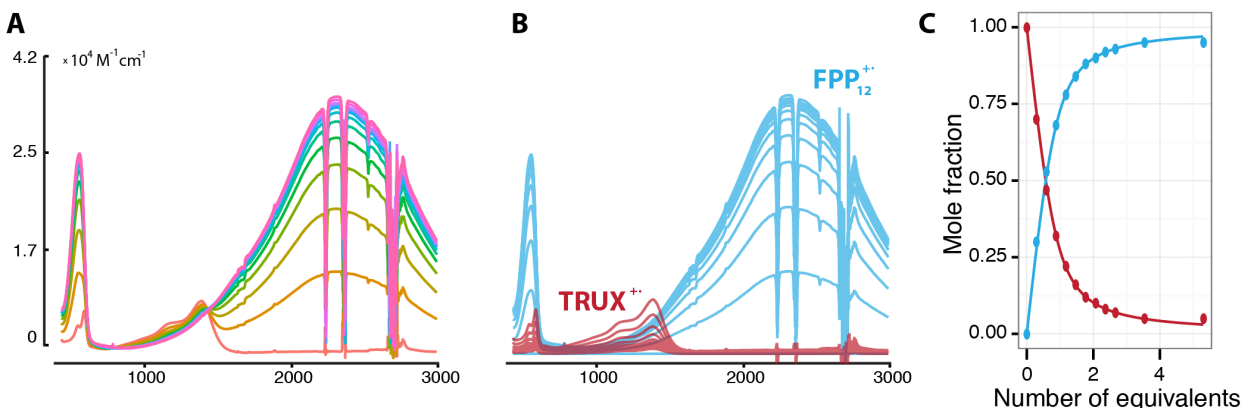


Figure S15. **A**: Spectral changes observed upon the reduction of 0.031 mM TRUX^{2+} in CH_2Cl_2 (3 mL) by addition of 15- μL increments of 0.4 mM solution of FPP_{10} in CH_2Cl_2 . **B**: Deconvolution of each UV-VIS absorption spectrum from figure **A** into its component spectra, i.e. TRUX^{2+} and FPP_{10}^{2+} . **C**: Plot of the mole fractions of TRUX^{2+} (red) and FPP_{10}^{2+} (blue) against the added equivalents of FPP_{10} . Symbols represent experimental points, while the solid lines show best-fit to experimental points using $\Delta G_1 = -53$ mV.

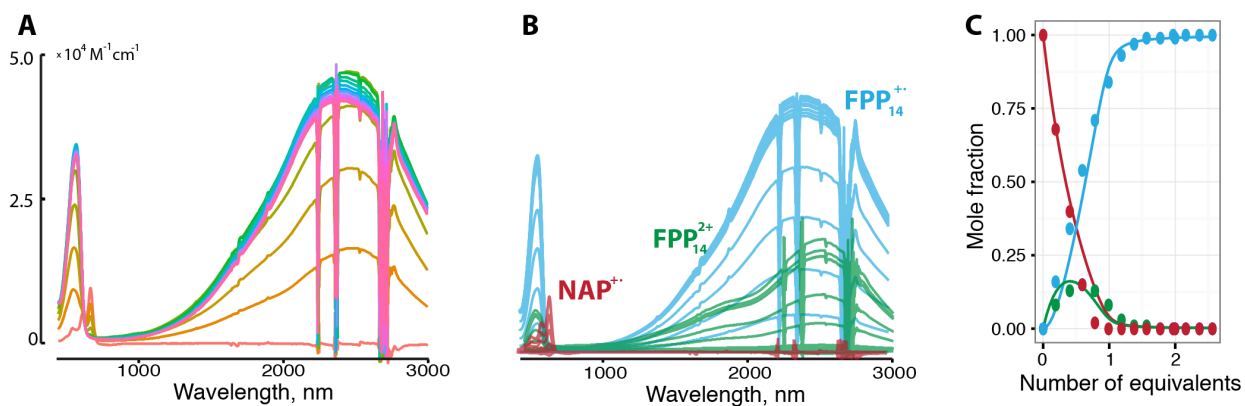


Figure S16. **A**: Spectral changes observed upon the reduction of 0.113 mM NAP^{2+} in CH_2Cl_2 (3 mL) by addition of 18- μL increments of 0.34 mM solution of FPP_{14} in CH_2Cl_2 . **B**: Deconvolution of each UV-VIS absorption spectrum from figure **A** into its component spectra, i.e. NAP^{2+} , FPP_{14}^{2+} and FPP_{14}^{+} . **C**: Plot of the mole fractions of NAP^{2+} (red), FPP_{14}^{2+} (green) and FPP_{14}^{+} (blue) against the added equivalents of FPP_{14} . Symbols represent experimental points, while the solid lines show best-fit to experimental points using $\Delta G_1 = -145$ mV and $\Delta G_{12} = 149$ mV.

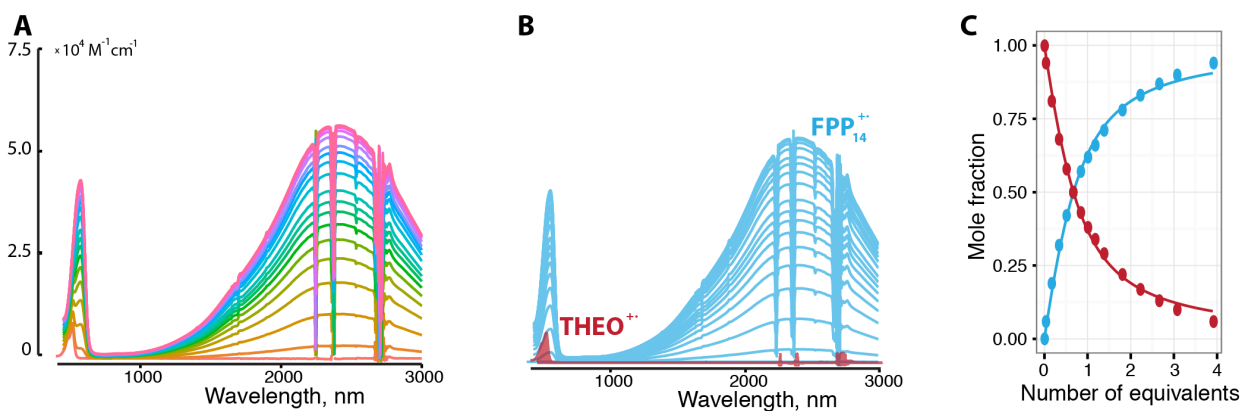


Figure S17. **A:** Spectral changes observed upon the reduction of 0.058 mM THEO^{++} in CH_2Cl_2 (3 mL) by addition of 15- μL increments of 0.68 mM solution of FPP_{12}^{++} in CH_2Cl_2 . **B:** Deconvolution of each UV-VIS absorption spectrum from figure A into its component spectra, i.e. THEO^{++} and FPP_{12}^{++} . **C:** Plot of the mole fractions of THEO^{++} (red) and FPP_{12}^{++} (blue) against the added equivalents of FPP_{12}^{++} . Symbols represent experimental points, while the solid lines show best-fit to experimental points using $\Delta G_1 = -27$ mV.

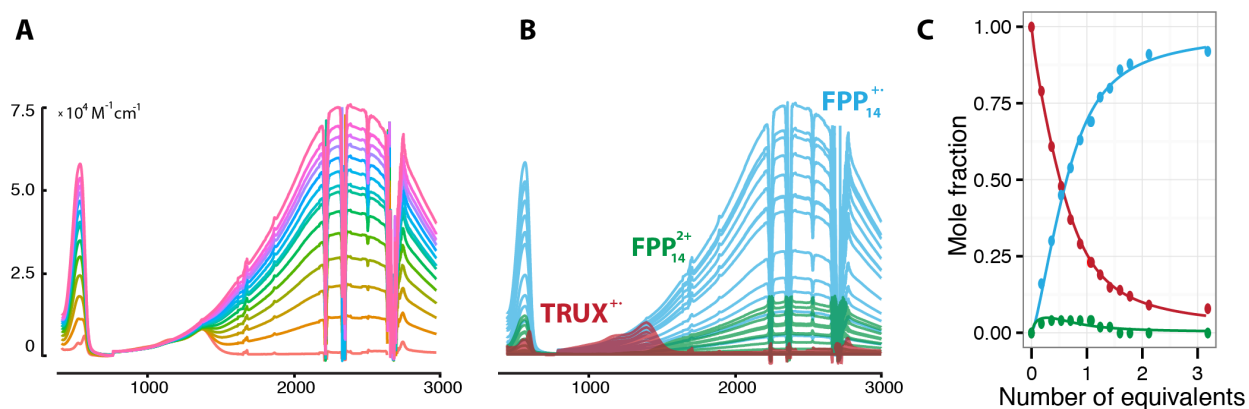


Figure S18. **A:** Spectral changes observed upon the reduction of 0.026 mM TRUX^{++} in CH_2Cl_2 (3 mL) by addition of 15- μL increments of 0.3 mM solution of FPP_{14}^{++} in CH_2Cl_2 . **B:** Deconvolution of each UV-VIS absorption spectrum from figure A into its component spectra, i.e. TRUX^{++} , FPP_{14}^{++} and FPP_{14}^{2+} . **C:** Plot of the mole fractions of TRUX^{++} (red), FPP_{14}^{++} (blue) and FPP_{14}^{2+} (green) against the added equivalents of FPP_{14}^{++} . Symbols represent experimental points, while the solid lines show best-fit to experimental points using $\Delta G_1 = -51$ mV and $\Delta G_{12} = 109$ mV.

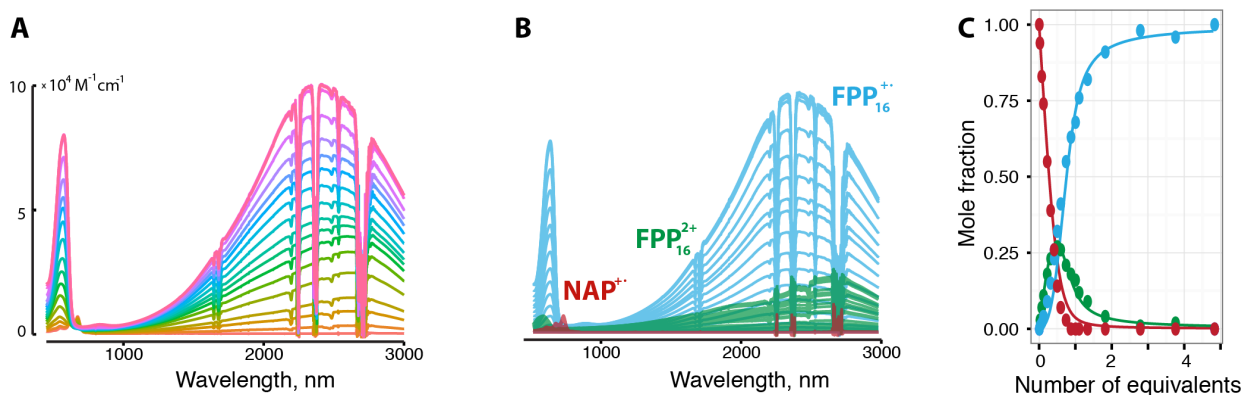


Figure S19. **A:** Spectral changes observed upon the reduction of 0.11 mM NAP^{++} in CH_2Cl_2 (3 mL) by addition of 18- μL increments of 0.16 mM solution of FPP_{16}^{++} in CH_2Cl_2 . **B:** Deconvolution of each UV-VIS absorption spectrum from figure A into

its component spectra, i.e. $\text{NAP}^{+\bullet}$, $\text{FPP}_{16}^{+\bullet}$ and FPP_{16}^{2+} . C: Plot of the mole fractions of $\text{NAP}^{+\bullet}$ (red), $\text{FPP}_{16}^{+\bullet}$ (blue) and FPP_{16}^{2+} (green) against the added equivalents of FPP_{16} . Symbols represent experimental points, while the solid lines show best-fit to experimental points using $\Delta G_1 = -122$ mV and $\Delta G_{12} = 83$ mV.

S3. Density Functional Theory (DFT) calculations

Computational details

The electronic structure calculations were performed using density functional theory (DFT) as implemented in Gaussian 09 package, revision D.01.⁸ An accurate description of the π -conjugated cation radicals is challenging for DFT because self-interaction error often leads to the artificial delocalization of the positive charge.^{9,10} In this work we used B1LYP-40/6-31G(d)^{11,12} level of theory with 40% contribution of the Hartree-Fock exchange term^{13,14} that was previously benchmarked against experimental data.¹⁵ Solvent effects were included using the implicit integral equation formalism polarizable continuum model (IEF-PCM)¹⁶⁻²⁰ with dichloromethane solvent parameters ($\epsilon = 8.93$). In all DFT calculations, ultrafine Lebedev's grid was used with 99 radial shells per atom and 590 angular points in each shell. Tight cutoffs on forces and atomic displacement were used to determine convergence in geometry optimization procedure. Harmonic vibrational frequency calculations were performed for the optimized structures to confirm absence of imaginary frequencies. For cation radicals, wavefunction stability tests²¹ were performed to ensure absence of solutions with lower energy. The values of $\langle S^2 \rangle$ operator after spin annihilation were confirmed to be close to the expectation value of 0.75. Unpaired spin density surface were obtained using isovalue of 0.001 a.u. Atomic charges were calculated using Natural Population Analysis approach.^{22,23} Calculations of the first excited state of FPP_n and $\text{FPP}_n^{+\bullet}$ were performed using the time-dependent density functional theory (TD-DFT) method.²⁴⁻²⁸

FPP_n in neutral and cation radical states

Neutral FPP_n

HOMO distribution in FPP_n

The equilibrium geometries of neutral FPP_n ($n = 2-18$) show that all *p*-phenylene units are structurally identical with the dihedral angle of $\sim 0.08 \pm 0.05^\circ$ within one fluorene unit and $\sim 37.15 \pm 0.11^\circ$ between two adjacent fluorenes. The HOMOs of neutral FPP_n are delocalized over the entire poly-*p*-phenylene chain following bell-shaped distribution with the maximum in the center of the chain (Figure S20). The HOMO ($\varphi_{\text{HOMO}} = \sum_k c_k \chi_k$ where c_k is a coefficient of atomic orbital χ_k) distribution are quantified by per-unit HOMO densities calculated as $q_m = \sum_n c_{mn}^2$ where m is index of *p*-phenylene unit and n is an index of atomic orbital in unit m . For the purpose of quantification, HOMO density distributions were fitted to the Gaussian function $e^{-\frac{(x-\mu)^2}{2\sigma^2}}$, where μ and σ are the center and width of the distribution. Here we use value of 3σ , which includes 99.7% of the distribution, to quantify the effective size of the HOMO density distribution (Table S3).

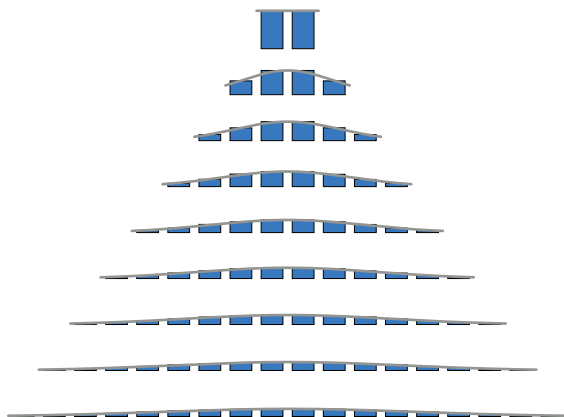


Figure S20. Barplot representations of the per-unit HOMO densities in FPP_n calculated using B1LYP-40/6-31G(d)+PCM(CH₂Cl₂).

Table S3. Center (mean value μ) and width (3σ , i.e. 99.7% of the distribution) of Gaussian distribution of the HOMO density. Count of the phenylene units start from 0. For example, $\mu = 0.5$ corresponds to the position between two units in FPP₂.

n	μ	3σ
2	0.5	--
4	1.5	4.3
6	2.5	5.0
8	3.5	6.3
10	4.5	7.4
12	5.5	8.7
14	6.5	9.9
16	7.5	11.1
18	8.5	12.3

Absorption energies of neutral FPP_n

The TD DFT calculations showed that the vertical excitation of neutral FPP_n to the first excited state is dominated by the HOMO→LUMO transition. The calculated excitation energies of FPP_n show an excellent agreement with the experimental energies ν_{abs} of the maximum absorption and follow a linear $\cos(\pi/(n+1))$ trend with no breakdown (Table S4, Figure S21).

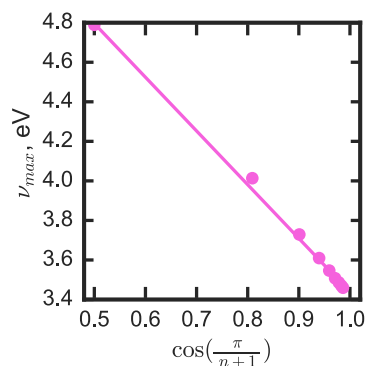


Figure S21. Plot of excitation energies (ν_{max}) to the first excited state calculated using TD B1LYP-40/6-31G(d)+PCM(CH_2Cl_2) level of theory against $\cos(\pi/(n+1))$ trend.

Table S4. Absorption energies ν_{abs} and oscillator strengths calculated for various FPP_n .

n	ν_{abs} , eV	ν_{abs} , nm	f_{osc}
2	4.79	259	0.44
4	4.01	309	1.58
6	3.73	332	2.59
8	3.61	343	3.56
10	3.55	350	4.52
12	3.51	353	5.45
14	3.49	356	6.32
16	3.47	357	7.24
18	3.46	358	8.07

Cation Radical $FPP_n^{+\bullet}$

Charge and spin-density distributions in $FPP_n^{+\bullet}$

To estimate the extent of hole delocalization we performed Natural Population Analysis (NPA) of various $FPP_n^{+\bullet}$. Per-unit distributions of the NPA charge and spin-densities indicate that the size of the hole is limited to several phenylene units (Figure S22). To quantify the extent of the hole delocalization, distributions of the charge and spin densities were fitted to Gaussian function $Ae^{-\frac{(x-\mu)^2}{2\sigma^2}}$, where μ and σ are the center and width of the distribution, A is amount of the charge/spin at the center of the distribution. Here we use value of 3σ , which includes 99.7% of the distribution, to quantify the effective size of the hole (Tables S5-S6).

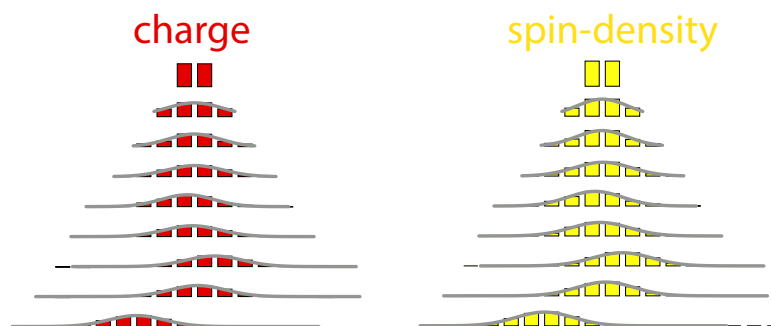


Figure S22. NPA charge and spin-density distributions in $FPP_n^{+\bullet}$ calculated using B1LYP-40/6-31G(d)+PCM(CH₂Cl₂) level of theory.

Table S5. Height A , center (mean value μ) and width (3σ , i.e. 99.7% of the distribution) of the Gaussian distribution of NPA charges in $FPP_n^{+\bullet}$.

n	μ	A	3σ
2	--	0.46	--
4	1.5	0.28	4.3
6	2.5	0.25	3.8
8	3.5	0.22	4.1
10	4.1	0.24	3.9
12	5.4	0.22	4.1
14	7.5	0.21	4.2
16	7.7	0.22	4.1
18	5.6	0.22	4.1

Table S6. Height A , center (mean value μ) and width (3σ , i.e. 99.7% of the distribution) of the Gaussian distribution of NPA spin-density in $FPP_n^{+\bullet}$.

n	μ	A	3σ
2	0.6	0.50	--
4	1.5	0.34	3.8
6	2.5	0.31	3.8
8	3.5	0.28	4.2
10	4.1	0.29	4.0

12	5.4	0.27	4.3
14	7.5	0.26	4.4
16	7.7	0.28	4.3
18	5.6	0.27	4.3

HOMO density distributions in neutral \mathbf{FPP}_n at the geometry of cation radical $\mathbf{FPP}_n^{+\bullet}$

The HOMOs of neutral \mathbf{FPP}_n are delocalized over the entire poly-*p*-phenylene chain and show a bell-shaped distribution with the maximum of HOMO density in the center of the chain as quantitatively visualized by the barplots (Figure S20). However, charge and spin-density distributions are delocalized over entire chain only for \mathbf{FPP}_2 – \mathbf{FPP}_8 , while in higher homologues the spin/charge distribution is limited to only ~ 8 *p*-phenylene units (Figure S22). At the same time, HOMOs of neutral \mathbf{FPP}_n at the structurally reorganized (cation-radical) geometries are similar to the spin/charge distributions (compare Figures S22 and S23). Note that the center of the HOMO density distribution matches the center of the hole distribution, however the HOMO density distribution is by a factor of 1.4 wider than the corresponding hole distributions.

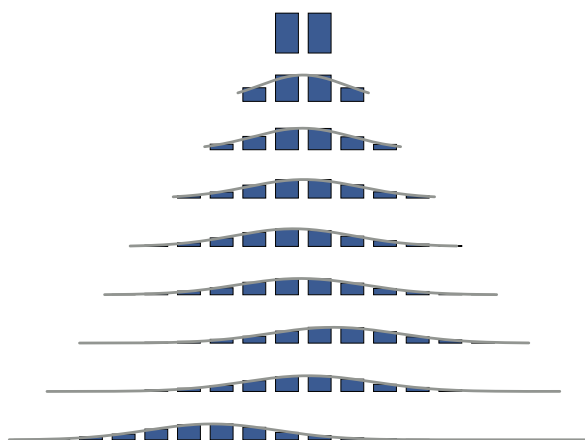


Figure S23. Per-unit barplot representations of HOMOs of neutral \mathbf{FPP}_n ($n = 2$ – 18) calculated at the equilibrium geometries of $\mathbf{FPP}_n^{+\bullet}$ calculated using B1LYP-40/6-31G(d)+PCM(CH₂Cl₂) level of theory.

Table S7. Height A , center (mean value μ) and width (3σ , i.e. 99.7% of the distribution) of the Gaussian distribution of HOMO density at the geometry of cation radical $\mathbf{FPP}_n^{+\bullet}$.

n	μ	A	3σ
2	0.5	0.495	--
4	1.5	0.327	4.0
6	2.5	0.267	4.5
8	3.5	0.230	5.2
10	4.2	0.219	5.5
12	5.4	0.202	5.8
14	7.4	0.196	5.9
16	7.7	0.195	5.9
18	5.7	0.197	5.9

Structural reorganization in $\text{FPP}_n^{+\bullet}$

Oxidation-induced changes in $\text{FPP}_n^{+\bullet}$ follow the nodal arrangement of HOMO resulting in the quinoidal distortion. Analysis of the equilibrium geometries of the $\text{FPP}_n^{+\bullet}$ cation radicals shows uneven structural reorganization that follows a bell-shaped distribution (Figure S24).

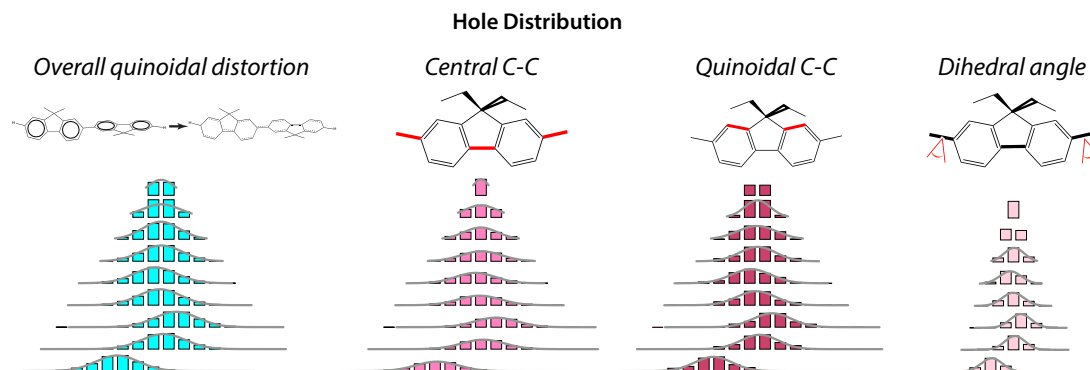


Figure S24. Barplot representation of the hole distribution in $\text{FPP}_n^{+\bullet}$ as measured by the changes (from equilibrium geometry in the neutral state) in central C-C bonds, aromatic (quinoidal) C-C bonds and dihedral angles between adjacent fluorenes.

To quantify the extent of the hole delocalization, distributions of the geometrical changes (from the neutral FPP_n) were fitted to Gaussian function $Ae^{-\frac{(x-\mu)^2}{2\sigma^2}}$, where μ and σ are the center and width of the distribution, A is amount of the distortion at the center of the distribution. Here we use value of 3σ , which includes 99.7% of the distribution, to quantify the effective size of the hole (Tables S18-S11). The quantification of the overall geometrical changes between neutral and cation radical FPP_n was obtained as a sum of relative changes of the central C-C bonds r_c between each pair of adjacent p -phenylenes and quinoidal C-C bonds r_q at each p -phenylene:

$$g_i = \frac{r_c^N(i) - r_c^{CR}(i)}{\langle r_c^N \rangle} + \frac{r_q^N(i) - r_q^{CR}(i)}{\langle r_q^N \rangle}$$

where g_i is an averaged geometrical change at the i th unit, $r_c^N(i) - r_c^{CR}(i)$ is the central C-C bond length change at i th unit, $r_q^N(i) - r_q^{CR}(i)$ is the quinoidal C-C bond length change at i th unit, $\langle r_c^N \rangle$ and $\langle r_q^N \rangle$ are averaged values of central and quinoidal C-C bonds of the neutral FPP_n .

Table S8. Height (A , in Å) and width (3σ , i.e. 99.7% of the distribution) of the Gaussian distribution of changes in central C-C bonds in the $\text{FPP}_n^{+\bullet}$.

n	A , Å	3σ
4	0.039	3.3
6	0.039	3.3
8	0.033	4.0
10	0.034	3.9
12	0.031	4.2
14	0.031	4.2
16	0.031	4.2
18	0.031	4.2

Table S9. Height (A , in Å) and width (3σ , i.e. 99.7% of the distribution) of the Gaussian distribution of changes in quinoidal C-C bonds in FPP_n^{++} .

n	A , Å	3σ
4	0.016	2.5
6	0.012	3.8
8	0.013	3.5
10	0.013	3.9
12	0.013	3.7
14	0.013	3.7
16	0.013	3.6

Table S10. Height (A , in degrees) and width (3σ , i.e. 99.7% of the distribution) of the Gaussian distribution of changes in dihedral angle between adjacent fluorenes in FPP_n^{++} .

n	A , °	3σ
6	11.1	--
8	14.6	2.0
10	13.0	2.1
12	13.6	2.1
14	14.3	2.1
16	14.3	2.0
18	14.0	2.1

Table S11. Center (mean value μ) and width (3σ , i.e. 99.7% of the distribution) of the Gaussian distribution of overall geometrical changes in the FPP_n^{++} .

n	μ	3σ
4	1.5	2.5
6	2.5	3.3
8	3.5	3.9
10	4.1	4.2
12	5.4	4.1
14	7.5	4.2
16	7.7	4.3
18	5.6	4.2

Oxidation and ionization potentials of FPP_n^{+}

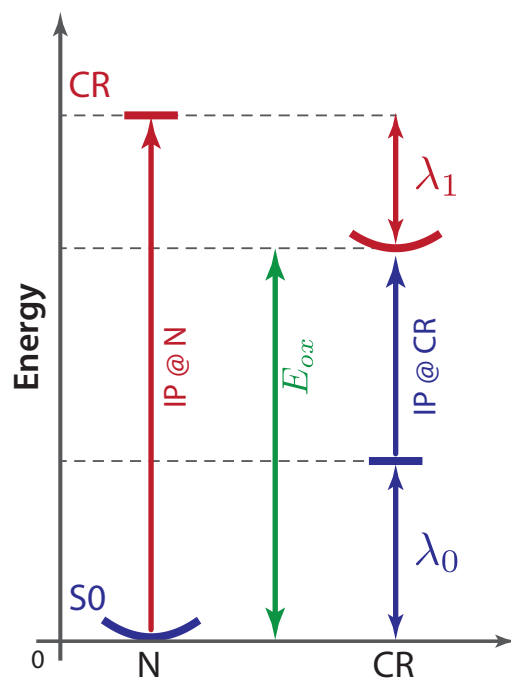


Figure S25. Schematic representation of various energetic properties: oxidation potential E_{ox} , ionization potentials (IP) at neutral and cation radical geometries, stabilization energy λ_1 in the cation radical state and reorganization penalty λ_0 in neutral state.

In accordance with the finite size of the hole distribution, evolution of the first oxidation potentials E_{ox1} follows a linear trend against $\cos(\pi/(n+1))$ only for small n and breaks down abruptly for larger n (Figure S26 and Table S12).

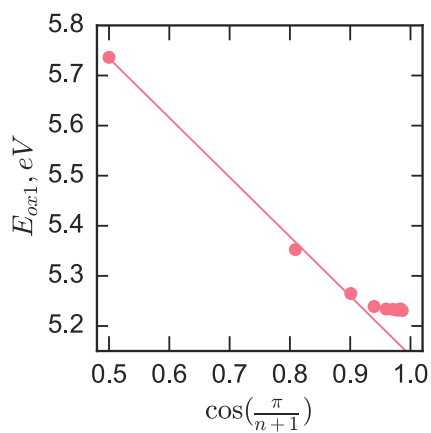


Figure S26. Evolution of the oxidation potentials E_{ox} of FPP_n calculated using B1LYP-40/6-31G(d)+PCM(CH_2Cl_2) level of theory against $\cos(\pi/(n+1))$ trend.

Table S12. Oxidation potentials E_{ox} of FPP_n calculated using B1LYP-40/6-31G(d)+PCM(CH_2Cl_2) level of theory against number of phenylene units.

n	E_{ox} , eV
2	5.74
4	5.35
6	5.26
8	5.24
10	5.23
12	5.23
14	5.23
16	5.23
18	5.23

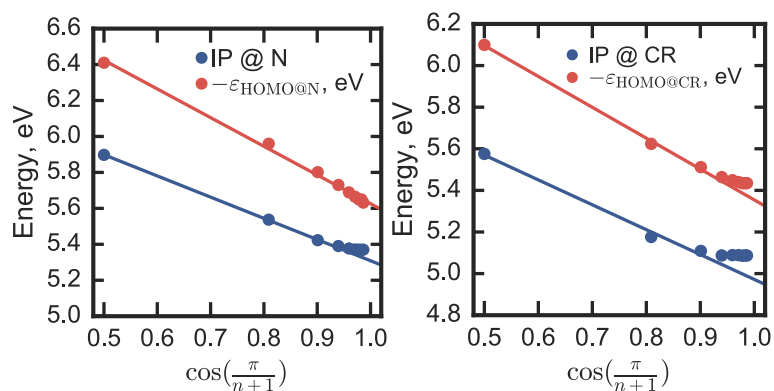


Figure S27. HOMO energies and ionization potentials of FPP_n at equilibrium geometries of neutral and cation radical states against $\cos(\pi/(n+1))$ trend calculated using B1LYP-40/6-31G(d)+PCM(CH_2Cl_2) level of theory.

Table S13. HOMO energies and ionization potentials of FPP_n at equilibrium geometries of neutral and cation radical states calculated using B1LYP-40/6-31G(d)+PCM(CH_2Cl_2) level of theory.

n	HOMO @ N, eV	IP @ N, eV	HOMO @ CR, eV	IP @ CR, eV
2	-6.41	5.90	-6.10	5.58
4	-5.96	5.54	-5.62	5.18
6	-5.80	5.42	-5.51	5.11
8	-5.73	5.39	-5.46	5.09
10	-5.69	5.38	-5.45	5.09
12	-5.66	5.37	-5.44	5.09
14	-5.65	5.37	-5.43	5.09
16	-5.65	5.37	-5.43	5.09
18	-5.63	5.37	-5.43	5.09

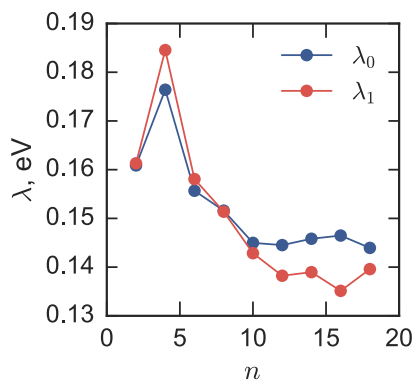


Figure 28. Energy λ_1 in the cation radical state and reorganization penalty λ_0 in neutral state of \mathbf{FPP}_n against number of phenylene units calculated using B1LYP-40/6-31G(d)+PCM(CH₂Cl₂) level of theory

Table S14. Energy λ_1 in the cation radical state and reorganization penalty λ_0 in neutral state of \mathbf{FPP}_n against number of phenylene units calculated using B1LYP-40/6-31G(d)+PCM(CH₂Cl₂) level of theory

n	λ_0 , eV	λ_1 , eV
2	0.161	0.161
4	0.176	0.185
6	0.156	0.158
8	0.152	0.151
10	0.145	0.143
12	0.145	0.138
14	0.146	0.139
16	0.146	0.135
18	0.144	0.140

Vertical excitation energies of \mathbf{FPP}_n^{++}

Evolution of the low-energy electronic excitation in \mathbf{FPP}_n^{++} , computed by means of TD-DFT, is also in an excellent agreement with experimental values and demonstrates linear $\cos(\pi/(n+1))$ trend up to 10-12 *p*-phenylene units (Figure S29) due to the more extensive delocalization of the hole in the vertically excited state D₁ as compared with the hole in the ground state D₀ (Figure S30). Starting from \mathbf{FPP}_{10}^{++} , ν_{\max} saturates, which corresponds well with the size of the charge distribution in the excited state.

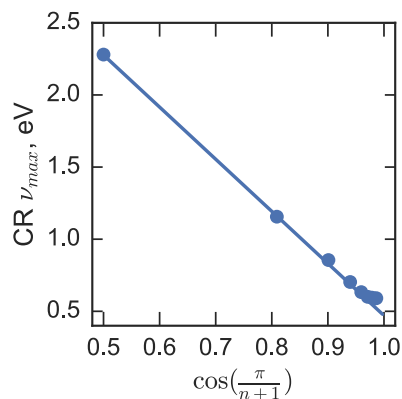


Figure S29. Evolution of the vertical excitation energies of FPP_n^{++} computed using B1LYP-40/6-31G(d)+PCM(CH₂Cl₂) level of theory against $\cos(\pi/(n+1))$ trend.

Table S15. Vertical excitation energies of FPP_n^{++} computed using B1LYP-40/6-31G(d)+PCM(CH₂Cl₂) level of theory against number of phenylene units.

n	CR v_{max} , eV
2	2.28
4	1.16
6	0.86
8	0.70
10	0.63
12	0.60
14	0.59
16	0.59
18	0.59

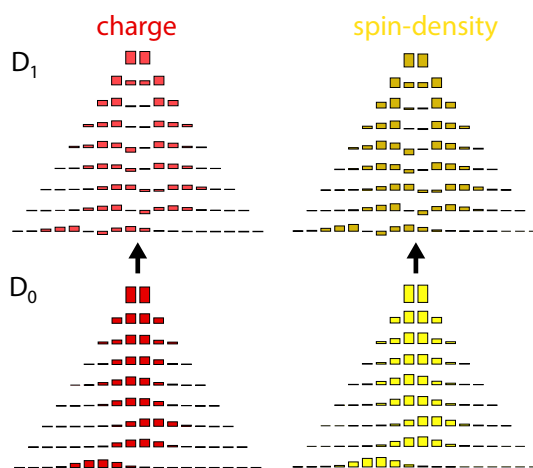


Figure S30. Per-unit barplot representations of the charge (red) and spin-density (yellow) distributions of FPP_n^{++} in ground (D_0) and first excited (D_1) states for $n = 1-9$.

DFT vs experimental results

Overall, the DFT results are in excellent agreement with experiment (Figure S31). The HOMOs of neutral \mathbf{FPP}_n are delocalized over the entire oligomer chain, which leads to the linear evolution of ν_{\max} against $\cos(\pi/(n+1))$ trend with no saturation. The hole distribution in $\mathbf{FPP}_n^{+\cdot}$ is compact and does not involve more than ~ 8 *p*-phenylene units in the ground state and ~ 10 units in the first excited state of $\mathbf{FPP}_n^{+\cdot}$. According to the saturation of the emission energy of \mathbf{FPP}_n , size of the exciton does not exceed ~ 10 *p*-phenylene units.

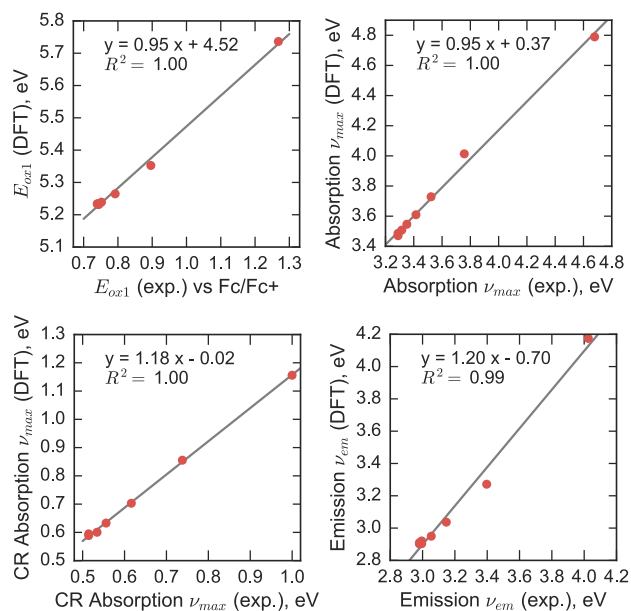


Figure S31. Comparison of the experimental first oxidation potential of \mathbf{FPP}_n , absorption maxima of \mathbf{FPP}_n and $\mathbf{FPP}_n^{+\cdot}$ and emission energies of \mathbf{FPP}_n with corresponding DFT values at B1LYP-40/6-31G(d)+PCM(DCM) level of theory.

S4. Particle-in-a-box model: comparison of $\cos[\pi/(n+1)]$ and $1/n$ trends

A systematic approach to study redox and optoelectronic properties of π -conjugated polymers involves measurement of the properties for successive series of oligomers, and subsequent extrapolation of these properties to the polymeric limit. Such studies of optical properties of neutral oligomers revealed a linear $\nu_{\max}(1/n)$ trend for both absorption and emission spectra, where n is the number of monomer units.³²⁻³⁴ One of the earliest explanations is based on the quantum-mechanical model of a particle in one-dimensional box applied to polyenes of length $L = l(n - 1)$ with n carbon atoms. Eigenvalues of the corresponding Hamiltonian are interpreted as energy levels of the molecular orbitals

$$E_k = \frac{h}{8ml^2} \frac{k^2}{(n-1)^2},$$

where E_k are energy levels of a particle, l is the length between two carbon atoms in the oligomer chain, m is the mass of the electron, and h is the Planck's constant. For a chain with n carbon atoms there are $n/2$ occupied orbitals (n is even) and HOMO/LUMO energies can be obtained as $\varepsilon_{HOMO} = E_{n/2}$ and $\varepsilon_{LUMO} = E_{n/2+1}$. Then, the HOMO-LUMO energy gap, which corresponds to the experimental ν_{\max} , is often scaled linearly with respect to $1/n$:

$$\nu_{\max} \approx \varepsilon_{LUMO} - \varepsilon_{HOMO} \approx \frac{h}{8ml^2} \frac{1}{n}$$

Despite the success of this model to describe properties of short oligomers, extrapolation to polymeric limit based on this trend may lead to incorrect results. For example, the experimental absorption energies of **FPP**_{*n*} follows a linear relationship with $1/n$ trend only up to $n \sim 4-5$ (Figure S32A). On the other hand, absorption energies are linear up to the polymeric limit when plotted against $\cos(\pi/(n+1))$ trend (Figure S32B). Indeed, comparison of the $1/n$ trend with the $\cos(\pi/(n+1))$ dependence shows that $1/n$ trend is linear with respect to $\cos(\pi/(n+1))$ trend up to $n \sim 6$ and deviates after $n \sim 10$ (Figure S32C).

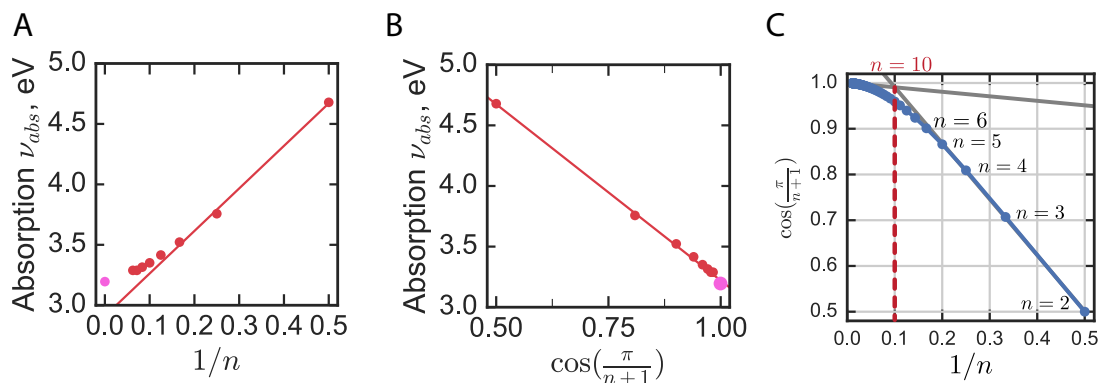


Figure S32. A: Experimental energies of maximum absorption of **FPP**_{*n*} against $1/n$ trend. B: Experimental energies of maximum absorption of **FPP**_{*n*} against $\cos(\pi/(n+1))$ trend. C: Comparison of $\cos(\pi/(n+1))$ trend with $1/n$ trend.

S5. Coarse-grained Hückel Molecular Orbital (HMO) theory

Here, we demonstrate advantages of Hückel Molecular Orbital (HMO) theory³⁵ to describe evolution of the redox and optical properties of poly-*p*-phenylene wires. Originally, HMO theory was applied to polyenes, where the Hamiltonian matrix is expressed in the basis of p_z atomic orbitals and accounts only for the fact of atomic adjacency and ignores actual geometric parameters. Since here we are interested in the evolution of redox and optical properties as a number of *p*-phenylene units in the chain, we represent molecular orbitals of the poly-*p*-phenylene as a linear combination of n HOMOs of the isolated *p*-phenylene units, referred to hereafter as a coarse-grained HMO theory:

$$\Psi = \sum_i^n c_i \varphi_i$$

where c_i is the expansion coefficient, φ_i is the HOMO of the isolated *p*-phenylene. At this point, we are not interested in the actual form of the atomic orbitals φ_i and how they can be obtained. However, we assume that these orbitals form an orthonormal basis such that $\int \varphi_i \varphi_j dv = \delta_{ij}$, where δ_{ij} is Kronecker symbol. We also require that the molecular orbitals Ψ are normalized, that is $|\Psi|^2 = \sum_i^n c_i^2 = 1$. Therefore, c_i^2 can be interpreted as the amount of electron localized at the i th unit in the chain. Then, for a HOMO Ψ we will refer c_i^2 as the HOMO density at the i th unit.

After substitution of the Ψ into the Schrödinger equation $H\Psi = \varepsilon\Psi$ and sequential multiplication by each φ_i followed by the integration over the entire space, we obtain an eigenvalue problem:

$$[\mathbf{H} - \varepsilon\mathbf{I}]\mathbf{c} = 0$$

where \mathbf{H} the Hamiltonian $n \times n$ matrix in the basis of HOMOs φ_i of isolated fragments, ε is the energy of the corresponding MO (also an eigenvalue of matrix \mathbf{H}), \mathbf{c} is the vector with coefficients c_i (also an eigenvector of matrix \mathbf{H}), \mathbf{I} is the identity matrix.

Following the Hückel's approximation we: neglect all interactions that do not involve adjacent units, take all diagonal elements to be the same, i.e. $H_{ii} = \alpha_H$ (HOMO energy of isolated fragment), and assume that the resonance integral (coupling) between two adjacent units is constant, i.e. $H_{ij} = \beta_H$. This results in the simplified $n \times n$ Hamiltonian matrix, also known as tight-binding Hamiltonian:

$$\mathbf{H} = \begin{bmatrix} \alpha_H & \beta_H & \cdots & 0 & 0 \\ \beta_H & \alpha_H & \cdots & 0 & 0 \\ \vdots & \vdots & \ddots & \vdots & \vdots \\ 0 & 0 & \cdots & \alpha_H & \beta_H \\ 0 & 0 & \cdots & \beta_H & \alpha_H \end{bmatrix},$$

where α_H is the HOMO energy of the non-interacting *p*-phenylene unit and β_H is the coupling between HOMOs of the adjacent *p*-phenylene units. The eigenvalues of this Hamiltonian matrix are known to have an analytical solution:

^{35,36}

$$\varepsilon_k = \alpha_H + 2\beta_H \cos\left(\frac{k\pi}{n+1}\right), k = 1, 2, \dots, n.$$

Because $\alpha < 0$ and $\beta < 0$, the eigenvalue ε_k with the smallest magnitude corresponds to the HOMO energy of poly-*p*-phenylene:

$$\varepsilon_{\text{HOMO}} = \alpha_{\text{H}} - 2\beta_{\text{H}} \cos\left(\frac{\pi}{n+1}\right)$$

Following the same protocol, LUMO energy of the poly-*p*-phenylene can be expressed as

$$\varepsilon_{\text{LUMO}} = \alpha_{\text{L}} + 2\beta_{\text{L}} \cos\left(\frac{\pi}{n+1}\right)$$

where α_{L} is the LUMO energy of the *p*-phenylene unit and β_{L} is the coupling between LUMOs of the adjacent *p*-phenylene units. Then, the HOMO-LUMO gap, which approximates the energy of maximum absorption, has a linear dependence with respect to $\cos\left(\frac{\pi}{n+1}\right)$:

$$\nu_{\text{max}} \approx \varepsilon_{\text{LUMO}} - \varepsilon_{\text{HOMO}} = \alpha_{\text{L}} - \alpha_{\text{H}} + 2(\beta_{\text{H}} + \beta_{\text{L}}) \cos\left(\frac{\pi}{n+1}\right).$$

Application of the presented HMO theory to **FPP_n** requires an improvement as the alternating orientation of the adjacent *p*-phenylenes in **FPP_n** imposes two different couplings: strong coupling β_{in} between two *p*-phenylenes in a single fluorene unit due to zero dihedral angle and a weaker coupling β_{out} between *p*-phenylenes in the adjacent fluorenes due to a larger dihedral angle ($\sim 37^\circ$). Therefore, here we use two different couplings in the Hückel Hamiltonian matrix:

$$\mathbf{H} = \begin{bmatrix} \alpha & \beta_{\text{in}} & 0 & \cdots & 0 & 0 & 0 \\ \beta_{\text{in}} & \alpha & \beta_{\text{out}} & \cdots & 0 & 0 & 0 \\ 0 & \beta_{\text{out}} & \alpha & \cdots & 0 & 0 & 0 \\ \vdots & \vdots & \vdots & \ddots & \vdots & \vdots & \vdots \\ 0 & 0 & 0 & \cdots & \alpha & \beta_{\text{out}} & 0 \\ 0 & 0 & 0 & \cdots & \beta_{\text{out}} & \alpha & \beta_{\text{in}} \\ 0 & 0 & 0 & \cdots & 0 & \beta_{\text{in}} & \alpha \end{bmatrix}$$

Numerical diagonalization of the Hückel Hamiltonian matrix produces a set of MO energies (i.e. eigenvalues) with corresponding coefficients of MOs (i.e. eigenvectors). HOMO energy α , and couplings β_{in} and β_{out} in matrix **H** require a parameterization with respect to the reference DFT values.

Parameterization of the coarse-grained HMO model of **FPP_n**

Benzene, a repetitive constituent in the poly-*p*-phenylene wire, has two degenerate HOMOs that are often termed as bisallylic and quinoidal orbitals (Figure S33). Interaction of these orbitals in a biphenyl (and also in **FPP₂**) leads to four MOs: HOMO and HOMO-3 are formed by the strong interaction between bisallylic orbitals of the monomers, while HOMO-1 and HOMO-2 are formed by a much weaker interaction between quinoidal orbitals of the monomers (Figure S34A).

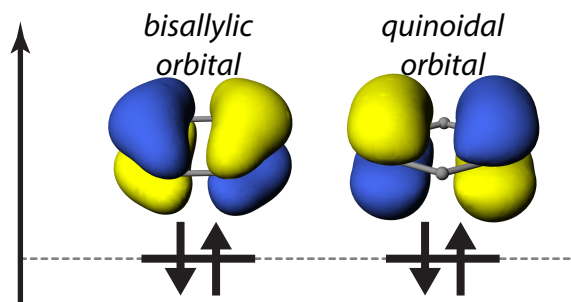


Figure S33. Two degenerate HOMOs of benzene: bisallylic and quinoidal

Thus, HOMO of the monomeric unit in the HMO model of \mathbf{FPP}_n can be approximated as a bisallylic orbital of the benzene (Figure S34). Coupling β can be approximated from the angular dependence of the splitting between HOMO and HOMO-3, which can be obtained from the scan of dihedral angle in biphenyl (Figure S34B). Then, for each dihedral angle in \mathbf{FPP}_n the coupling β was determined from the obtained angular dependence. From this parameterization, energy of the monomer $\alpha = -7.41 \text{ eV}$ and couplings $\beta_{in} = -0.95 \text{ eV}$ and $\beta_{out} = -0.75 \text{ eV}$.

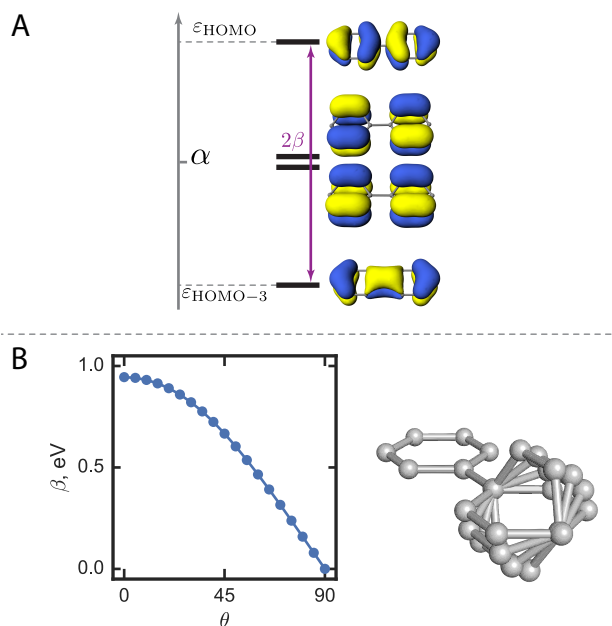


Figure S34. A: Molecular orbital diagram of biphenyl. Coupling β is estimated from the splitting of the (bisallylic) HOMO and HOMO-3. B: For each value of dihedral angle in \mathbf{FPP}_n coupling β can be estimated from the angular dependence in biphenyl.

Using the parameterized values, Hückel Hamiltonian matrices were constructed for each \mathbf{FPP}_n ($n = 1-9$) and numerically diagonalized. Diagonalization produced the MO energies ε_i (i.e. eigenvalues) and the corresponding MO density distributions (i.e. eigenvectors), where the eigenvalue with the smallest magnitude corresponds to the HOMO energy $\varepsilon_{\text{HOMO}}$ of each \mathbf{FPP}_n , while coefficient c_i^2 in the eigenvector represents HOMO density at the i th unit.

Due to the presence of two different couplings, energies of MOs from HMO theory form two bands: splitting between two bands is defined by the larger coupling β_{in} , while orbitals splitting within each band is defined by the

smaller coupling β_{out} (Figure S35). The eigenvalue with the smallest magnitude corresponds to the HOMO energy and evolves linearly with the $\cos(\pi/(n + 1))$ (Figure S36). HOMO energies obtained from the parameterized HMO theory are in excellent agreement with the DFT results (Figure S37 left).

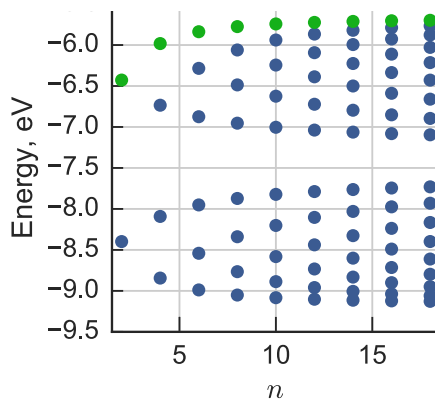


Figure S35. Occupied MOs of various FPP_n predicted by the HMO theory. HOMO energies are highlighted with green color.

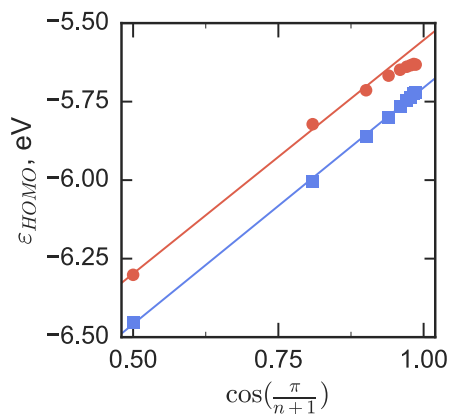


Figure S36. Evolution of HOMO energies obtained with the parameterized HMO theory. Two case are shown: HMO theory with the unperturbed energies of monomeric HOMOs (blue) and HMO theory with the monomeric HOMOs elevated according to the charge distribution in FPP_n^{++} (red).

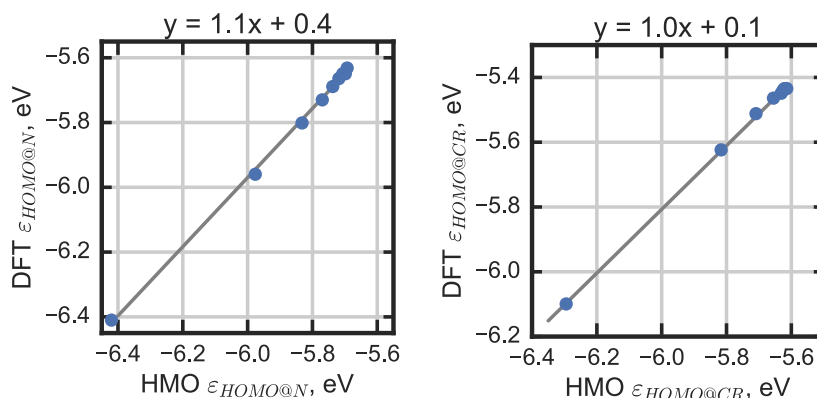


Figure S37. Linear correlation between MO energies obtained with DFT and HMO theory. Two case are shown: HMO theory with the unperturbed energies of monomeric HOMOs (left) and HMO theory with the monomeric HOMOs elevated according to the charge distribution in $\mathbf{FPP}_n^{+\bullet}$ (right).

Inclusion of structural reorganization in the HMO theory

In case of a single benzene ring, upon $1-e^-$ oxidation, HOMO energy of the neutral state at the reorganized geometry is elevated by $\Delta\alpha = 0.3 \text{ eV}$ (Figure S38). Thus, to account for the structural reorganization due to $1-e^-$ oxidation of \mathbf{FPP}_n , HOMO energies α of the monomers can be elevated proportionally to the amount of charge at each unit in $\mathbf{FPP}_n^{+\bullet}$:

$$\Delta\alpha_i = q_i\Delta\alpha$$

where $\Delta\alpha_i$ is amount by which the HOMO energy of the respective unit should be elevated, q_i is amount of charge at the unit and $\Delta\alpha = 0.3 \text{ eV}$ is the HOMO energy elevation in the fully oxidized unit.

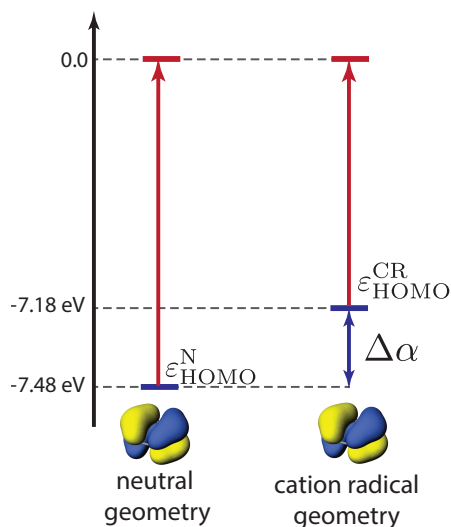


Figure S38. HOMO energy diagram of neutral state of benzene at neutral and cation radical geometries.

Electronic couplings β_{out} between each pair of adjacent fluorenes can be adjusted according to the angular dependence (Figure S34B):

$$\beta_{out}(\varphi) = \beta_0 \cos \varphi$$

where β_0 is the coupling between monomeric HOMOs at zero dihedral angle, φ is a dihedral angle between adjacent fluorenes. As the result, the modified Hückel Hamiltonian matrix takes into account structural reorganization using different couplings (β_{out}) and elevated HOMO energies (α_i) of the respective units:

$$\mathbf{H} = \begin{bmatrix} \alpha_1 & \beta_{in} & 0 & \dots & 0 & 0 & 0 \\ \beta_{in} & \alpha_2 & \beta_0 \cos \varphi_1 & \dots & 0 & 0 & 0 \\ 0 & \beta_0 \cos \varphi_1 & \alpha_3 & \dots & 0 & 0 & 0 \\ \vdots & \vdots & \vdots & \ddots & \vdots & \vdots & \vdots \\ 0 & 0 & 0 & \dots & \alpha_{n-2} & \beta_0 \cos \varphi_{n/2} & 0 \\ 0 & 0 & 0 & \dots & \beta_0 \cos \varphi_{n/2} & \alpha_{n-1} & \beta_{in} \\ 0 & 0 & 0 & \dots & 0 & \beta_{in} & \alpha_n \end{bmatrix}$$

According to the Koopmans' paradigm, HOMO energy and HOMO density distributions obtained from the diagonalization of the modified Hamiltonian matrix, respectively approximate oxidation potential and charge distribution of FPP_n^{+} .

Table S16. Height A , center (mean value μ) and width (3σ , i.e. 99.7% of the distribution) of the Gaussian distribution of HOMO density obtained from the HMO theory with modified Hamiltonian.

n	μ	A	3σ
2	0.5	0.500	--
4	1.5	0.361	3.4
6	2.5	0.284	4.2
8	3.5	0.244	4.9
10	4.2	0.223	5.4
12	5.4	0.202	5.9
14	7.4	0.194	6.1
16	7.6	0.186	6.3
18	5.8	0.191	6.1

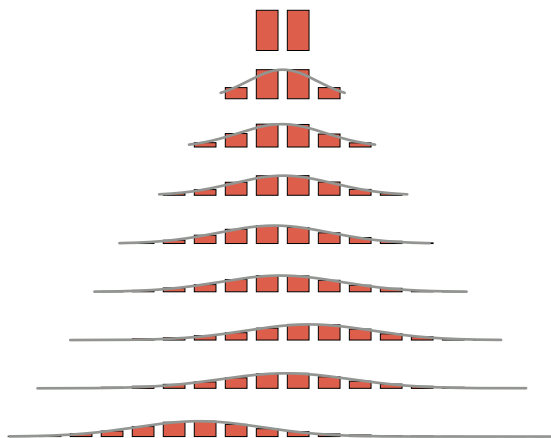


Figure S39. Per-unit barplot representations of HOMOs of FPP_n ($n = 2-18$) obtained from the HMO theory with modified Hamiltonian.

S6. Multi-State Model (MSM)

Let us introduce continuous reaction coordinate x along the poly- p -phenylene cation radical that represents structural/solvent reorganization. By solving the Schrodinger equation at each value of x , one can obtain the potential energy surface $E(x)$ along the reaction coordinate:

$$H(x)\Psi(x) = E(x)\Psi(x),$$

where Hamiltonian $H(x)$ parametrically depends on the coordinate x , $E(x)$ is adiabatic potential energy surface and $\Psi(x)$ is the wavefunction of the the poly- p -phenylene cation radical. Wavefunction $\Psi(x)$ can be expanded as a linear combination of the orthonormal basis functions ψ_i :

$$\Psi(x) = \sum_i^n c_i(x)\psi_i$$

where ψ_i represents wavefunction of the poly- p -phenylene cation radical with the positive charge localized at the i th unit. At this point we are not interested in the actual form of the basis functions ψ_i and how they can be obtained, however we require that these basis functions ψ_i form an orthonormal basis and that $\Psi(x)$ is a normalized function, i.e. $|\Psi|^2 = \sum_i^n c_i^2 = 1$. Then, for a given position x , coefficients c_i^2 represent the amount of the hole that occupies i th unit in the oligomer.

After substitution of the $\Psi(x)$ into the Schrödinger equation and sequential multiplication by each ψ_i followed by the integration over the entire space, we obtain an eigenvalue problem:

$$[\mathbf{H}(x) - E(x)\mathbf{I}]\mathbf{c} = 0$$

where $\mathbf{H}(x)$ is the Hamiltonian $n \times n$ matrix in the basis of ψ_i , $E(x)$ is the adiabatic potential energy surface with respect to the charge transfer coordinate x , \mathbf{c} is the vector with coefficients c_i (also an eigenvector of matrix \mathbf{H}), \mathbf{I} is the identity matrix. Here, we represent the Hamiltonian matrix in the tight-binding form where diagonal elements represent the diabatic surfaces $H_i(x)$ and upper/lower diagonals represent the couplings between adjacent diabatic states.

In case of poly-*p*-phenylene wire, complete oxidation of the *p*-phenylene unit (e.g. *i*th unit with coordinate x_i) leads to the quinoidal distortions of this unit and accumulation of the negative charge from the solvent around the unit. Then, with the geometry of the wire and solvent arrangement being fixed, a variation of the charge coordinate x in the vicinity of the reorganized unit leads to the quadratic increase in energy, while at a larger separation distance (i.e. $x - x_i$) the energy reaches a finite value following the Coulomb law of the electrostatic interaction.³⁷ Accordingly, the diabatic state $H_i(x)$ can be represented as a bell-shaped continuous function of the charge coordinate x using the composite quadratic/reciprocal dependence:³⁷

$$H_i(x) = \begin{cases} \lambda(x - x_i)^2, & \text{if } |x - x_i| \leq t \\ \lambda^\infty - a/|x - x_i|, & \text{if } |x - x_i| \geq t \end{cases}$$

where λ is the structural reorganization, λ^∞ is the energy of the completely separated hole and reorganization, parameters $t = \sqrt{\lambda^\infty/3\lambda}$ and $a = 2\lambda t^3$ are defined by the continuity of $H_i(x)$ and its first derivative. Parameter t defines a separation distance after which the interaction mechanism switches from the short-range to the long-range interaction.

Application of MSM to \mathbf{FPP}_n^{++} ,

In case of \mathbf{FPP}_n^{++} , alternation of the dihedral angles between *p*-phenylenes within a fluorene and between adjacent fluorenes requires use of alternating coupling H_{in}^{ab} and H_{out}^{ab} . Thus, the Hamiltonian matrix can be represented as:

$$\mathbf{H}(x) = \begin{bmatrix} H_1(x) & H_{in}^{ab} & 0 & \cdots & 0 & 0 & 0 \\ H_{in}^{ab} & H_2(x) & H_{out}^{ab} & \cdots & 0 & 0 & 0 \\ 0 & H_{out}^{ab} & H_3(x) & \cdots & 0 & 0 & 0 \\ \vdots & \vdots & \vdots & \ddots & \vdots & \vdots & \vdots \\ 0 & 0 & 0 & \cdots & H_{n-2}(x) & H_{in}^{ab} & 0 \\ 0 & 0 & 0 & \cdots & H_{in}^{ab} & H_{n-1}(x) & H_{out}^{ab} \\ 0 & 0 & 0 & \cdots & 0 & H_{out}^{ab} & H_n(x) \end{bmatrix}$$

Numerical diagonalization of the Hamiltonian matrix $\mathbf{H}(x)$ for each x results in the adiabatic potential energy surface with the lowest-energy surface $E_0(x)$ corresponding to the ground state of \mathbf{FPP}_n^{++} . The minimum on the ground state surface $E_0(x)$ defines the position x_{min} of the center of the hole distribution and the energy at this point $E_0(x_{min})$ directly corresponds to the oxidation potential E_{ox1} of \mathbf{FPP}_n . Parameters $\lambda, \lambda^\infty, H_{in}^{ab}, H_{out}^{ab}$ were adjusted until the MSM provided oxidation energies, $D_0 \rightarrow D_1$ transitions and charge distributions of \mathbf{FPP}_n^{++} similar to those obtained by DFT and/or experiment. The optimized parameters of \mathbf{FPP}_n^{++} are $\lambda = 2, \lambda^\infty = 12, H_{in}^{ab} = 19, H_{out}^{ab} = 15$.

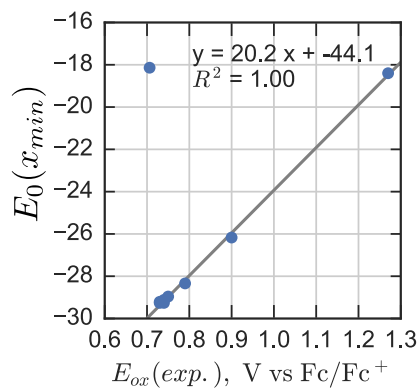


Figure S40. Comparison of the experimental oxidation potentials E_{ox} and stabilization energies $E_0(x_{min})$ from MSM.

Table S17. Center (mean value μ) and width (3σ , i.e. 99.7% of the distribution) of the Gaussian distribution of the hole distribution in the FPP_n^{+} obtained from MSM.

n	μ	3σ
2	0.5	72.2
4	1.5	3.3
6	2.6	3.5
8	3.1	3.9
10	4.2	4.0
12	6.1	4.1
14	8.1	4.1
16	8.9	4.1
18	6.1	4.1

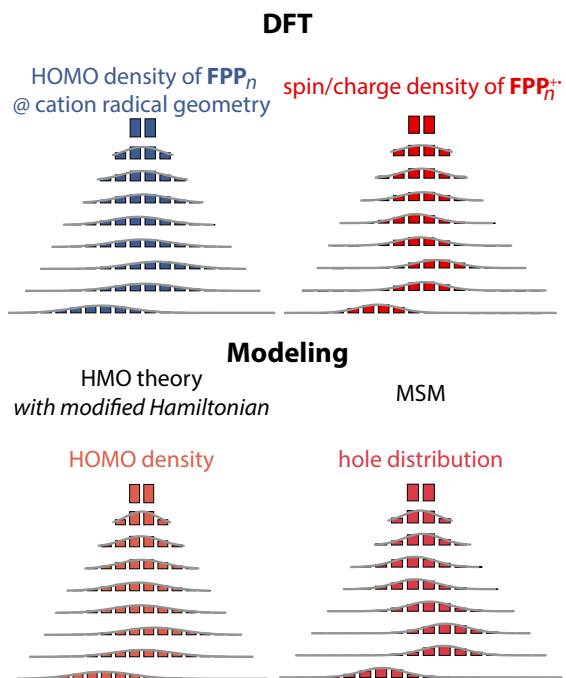


Figure S41. Comparison of the charge/spin density distributions and HOMO density of neutral \mathbf{FPP}_n at cation radical geometry obtained from DFT with the corresponding distributions obtained from the modeling: HOMO density from HMO theory with modified Hamiltonian and hole distribution from MSM ($\lambda = 2, \lambda^\infty = 12, H_{in}^{ab} = 19, H_{out}^{ab} = 15$).

S7. Equilibrium geometrical parameters of FPP_n in neutral and cation radical states

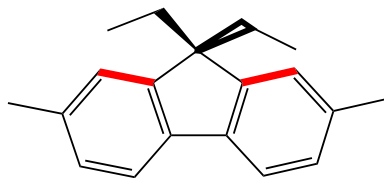
Table S18. Equilibrium central C-C bonds in neutral and cation radical states of FPP_n calculated at B1LYP-40/6-31G(d)+PCM(DCM) level of theory.



<i>n</i>	<i>i</i>	$r_N, \text{Å}$	$r_{CR}, \text{Å}$	$r_N - r_{CR}, \text{pm}$
2	1	1.467	1.414	5.29
	1	1.465	1.439	2.59
4	2	1.482	1.442	3.94
	3	1.465	1.439	2.58
6	1	1.465	1.456	0.95
	2	1.482	1.458	2.35
	3	1.464	1.425	3.88
	4	1.482	1.459	2.27
	5	1.465	1.456	0.90
8	1	1.465	1.462	0.29
	2	1.482	1.473	0.88
	3	1.463	1.437	2.61
	4	1.481	1.449	3.28
	5	1.463	1.436	2.70
	6	1.482	1.472	0.92
	7	1.465	1.462	0.30
10	1	1.465	1.464	0.14
	2	1.482	1.477	0.45
	3	1.463	1.447	1.62
	4	1.481	1.454	2.76
	5	1.463	1.429	3.41
	6	1.481	1.464	1.73
	7	1.463	1.456	0.80
	8	1.482	1.480	0.18
	9	1.465	1.465	0.05
12	1	1.465	1.465	0.03
	2	1.482	1.481	0.09
	3	1.464	1.459	0.42
	4	1.481	1.471	1.05
	5	1.463	1.436	2.76

	6	1.481	1.450	3.13
	7	1.463	1.439	2.45
	8	1.481	1.473	0.87
	9	1.463	1.460	0.35
	10	1.482	1.481	0.07
	11	1.465	1.465	0.02
<hr/>				
	1	1.465	1.465	0.01
	2	1.482	1.481	0.00
	3	1.464	1.463	0.03
	4	1.481	1.481	0.09
	5	1.463	1.459	0.40
	6	1.481	1.472	0.98
14	7	1.463	1.437	2.61
	8	1.481	1.450	3.13
	9	1.463	1.437	2.59
	10	1.481	1.472	0.94
	11	1.463	1.460	0.37
	12	1.482	1.481	0.08
	13	1.465	1.465	0.02
<hr/>				
	1	1.465	1.465	0.00
	2	1.482	1.481	0.00
	3	1.464	1.463	0.04
	4	1.481	1.481	0.07
	5	1.463	1.460	0.31
	6	1.481	1.473	0.81
	7	1.464	1.440	2.38
16	8	1.481	1.450	3.11
	9	1.463	1.435	2.82
	10	1.481	1.470	1.12
	11	1.463	1.459	0.47
	12	1.481	1.480	0.10
	13	1.464	1.463	0.04
	14	1.482	1.481	0.00
	15	1.465	1.465	0.00
<hr/>				

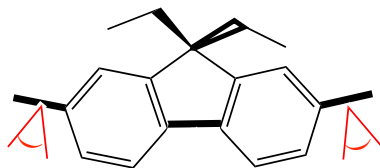
Table S19. Equilibrium quinoidal C-C bonds in neutral and cation radical states of **FPP_n**, calculated at B1LYP-40/6-31G(d)+PCM(DCM) level of theory.



<i>n</i>	<i>i</i>	r_{N_i} , Å	r_{CR_i} , Å	$r_{N_i}-r_{CR_i}$, pm
2	1	1.385	1.376	0.95
	2	1.385	1.376	0.95
4	1	1.385	1.383	0.19
	2	1.382	1.367	1.57
	3	1.382	1.367	1.58
	4	1.385	1.383	0.20
6	1	1.385	1.385	0.03
	2	1.382	1.375	0.75
	3	1.382	1.370	1.24
	4	1.382	1.370	1.20
	5	1.382	1.375	0.71
	6	1.385	1.385	0.03
8	1	1.385	1.385	0.00
	2	1.382	1.380	0.25
	3	1.382	1.377	0.49
	4	1.382	1.369	1.32
	5	1.382	1.369	1.34
	6	1.382	1.377	0.51
	7	1.382	1.380	0.27
	8	1.385	1.385	0.00
10	1	1.385	1.385	-0.01
	2	1.382	1.381	0.13
	3	1.382	1.380	0.23
	4	1.382	1.372	0.98
	5	1.382	1.369	1.30
	6	1.382	1.373	0.92
	7	1.382	1.377	0.55
	8	1.382	1.381	0.08
	9	1.382	1.382	0.06
	10	1.385	1.385	-0.01
12	1	1.385	1.385	0.00
	2	1.382	1.382	0.03
	3	1.382	1.382	0.03

	4	1.382	1.379	0.32
	5	1.382	1.376	0.58
	6	1.382	1.369	1.30
	7	1.382	1.370	1.25
	8	1.382	1.377	0.47
	9	1.382	1.380	0.26
	10	1.382	1.382	0.01
	11	1.382	1.382	0.03
	12	1.385	1.385	0.00
	<hr/>			
	1	1.385	1.385	0.00
	2	1.382	1.382	0.00
	3	1.382	1.382	0.00
	4	1.382	1.382	0.03
	5	1.382	1.382	0.03
	6	1.382	1.379	0.29
14	7	1.382	1.377	0.54
	8	1.382	1.369	1.29
	9	1.382	1.369	1.27
	10	1.382	1.377	0.49
	11	1.382	1.379	0.28
	12	1.382	1.382	0.03
	13	1.382	1.382	0.02
	14	1.385	1.385	0.00
	<hr/>			
	1	1.385	1.385	0.00
	2	1.382	1.382	0.00
	3	1.382	1.382	0.00
	4	1.382	1.382	0.02
	5	1.382	1.382	0.02
	6	1.382	1.380	0.24
	7	1.382	1.378	0.42
	8	1.382	1.370	1.22
16	9	1.382	1.369	1.34
	10	1.382	1.376	0.62
	11	1.382	1.379	0.34
	12	1.382	1.382	0.04
	13	1.382	1.382	0.04
	14	1.382	1.382	-0.01
	15	1.382	1.382	0.01
	16	1.385	1.385	0.00
	<hr/>			

Table 20. Equilibrium dihedral angle between adjacent phenylenes in neutral and cation radical states of FPP_n calculated at B1LYP-40/6-31G(d)+PCM(DCM) level of theory.



n	i	$\theta_{N_s}, ^\circ$	$\theta_{CR_s}, ^\circ$	$\theta_{N_s} - \theta_{CR_s}, ^\circ$
2	1	0.0	0.0	0.0
	1	0.2	0.3	-0.1
4	2	37.4	20.1	17.3
	3	0.2	0.3	-0.1
6	1	0.2	0.3	-0.1
	2	37.3	26.2	11.1
	3	0.1	0.0	0.1
	4	-36.9	-27.1	-9.8
	5	-0.2	-0.2	0.1
8	1	0.1	0.2	-0.1
	2	37.0	32.9	4.1
	3	0.0	0.1	-0.1
	4	-37.1	-22.5	-14.6
	5	0.1	0.2	-0.1
	6	37.6	32.5	5.1
10	7	0.2	0.3	-0.1
	1	0.1	0.2	0.0
	2	36.9	35.0	1.8
	3	-0.1	0.0	-0.1
	4	-37.3	-24.3	-13.0
	5	0.0	-0.2	0.1
	6	37.2	28.8	8.4
	7	0.0	0.1	-0.1
	8	-37.1	-36.2	-0.9
9	-0.2	-0.1	0.0	
12	1	0.2	0.1	0.0
	2	37.2	36.9	0.3
	3	0.0	0.0	0.0
	4	-36.7	-31.4	-5.3
	5	0.0	0.4	-0.4
	6	37.1	23.5	13.6
	7	0.0	0.3	-0.2
	8	-37.1	-32.4	-4.7
	9	0.0	0.0	-0.1

	10	36.9	36.7	0.2
	11	0.1	0.2	0.0
<hr/>				
	1	0.2	0.2	0.0
	2	37.4	37.3	0.1
	3	0.0	0.0	0.0
	4	-36.8	-36.4	-0.4
	5	0.0	0.0	0.0
	6	37.2	31.9	5.3
14	7	0.0	0.1	-0.1
	8	-37.2	-22.9	-14.3
	9	0.0	0.1	-0.1
	10	36.9	32.2	4.6
	11	0.0	0.1	-0.1
	12	-37.1	-36.5	-0.6
	13	-0.2	-0.2	0.0
<hr/>				
	1	-0.2	-0.1	0.0
	2	-37.1	-37.1	0.1
	3	0.0	0.0	0.0
	4	-142.9	-143.5	0.6
	5	0.0	-0.2	0.2
	6	-37.0	-33.5	-3.5
	7	0.0	-0.3	0.3
16	8	37.2	22.8	14.3
	9	0.0	0.1	-0.1
	10	-37.0	-31.4	-5.6
	11	0.0	0.0	0.0
	12	37.2	36.6	0.5
	13	0.0	0.0	0.0
	14	-37.1	-36.9	-0.2
	15	-0.2	-0.2	0.0
<hr/>				

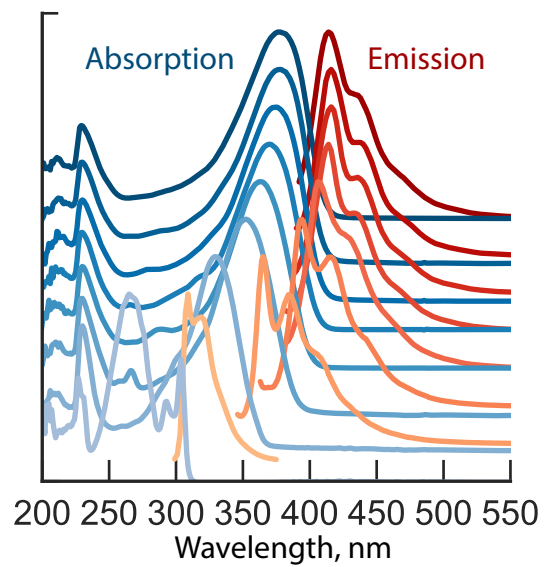


Figure S42. Compilation of the normalized absorption and emission spectra of \mathbf{FPP}_n in CH_2Cl_2 at 22 °C.

S8. References

- (1) Zhai, L.; Shukla, R.; Wadumethrige, S. H.; Rathore, R. Probing the Arenium-ion (protontransfer) Versus the Cation-radical (electron Transfer) Mechanism of Scholl Reaction Using DDQ As Oxidant. *J. Org. Chem.* **2010**, *75*, 4748-4760.
- (2) Rathore, R.; Burns, C. L.; Deselnicu, M. I. Preparation of 1, 4: 5, 8-Dimethano-1, 2, 3, 4, 5, 6, 7, 8-Octahydro-9, 10-Dimethoxyanthracenium Hexachloroantimonate (4+ SbCl₆⁻): A Highly Robust Radical-Cation Salt. *Org. Synth.* **2005**, 1-9.
- (3) Rathore, R.; Kochi, J. K. Acid Catalysis Vs. Electron-transfer Catalysis Via Organic Cations or Cation-radicals As the Reactive Intermediate. Are These Distinctive Mechanisms? *Acta. Chem. Scand.* **1998**, *52*, 114-130.
- (4) Rathore, R.; Burns, C. L.; Deselnicu, M. I. Multiple-electron Transfer in a Single Step. Design and Synthesis of Highly Charged Cation-radical Salts. *Org. Lett.* **2001**, *3*, 2887-2890.
- (5) Rathore, R.; Kochi, J. K. Acid Catalysis Vs. Electron-transfer Catalysis Via Organic Cations or Cation-radicals As the Reactive Intermediate. Are These Distinctive Mechanisms? *Acta. Chem. Scand.* **1998**, *52*, 114-130.
- (6) Talipov, M. R.; Boddeda, A.; Hossain, M. M.; Rathore, R. Quantitative Generation of Cation Radicals and Dications Using Aromatic Oxidants: Effect of Added Electrolyte on the Redox Potentials of Aromatic Electron Donors. *J. Phys. Org. Chem.* **2015**, *29*, 227-233.
- (7) Talipov, M. R.; Hossain, M. M.; Boddeda, A.; Thakur, K.; Rathore, R. A Search for Blues Brothers: X-ray Crystallographic/spectroscopic Characterization of the Tetraarylbenzidine Cation Radical As a Product of Aging of Solid Magic Blue. *Org. Biomol. Chem.* **2016**, *14*, 2961-2968.
- (8) Frisch, M. J.; Trucks, G. W.; Schlegel, H. B.; Scuseria, G. E.; Robb, M. A.; Cheeseman, J. R.; Scalmani, G.; Barone, V.; Mennucci, B.; Petersson, G. A.; et. al. Gaussian, Inc., Wallingford CT, 2009.
- (9) Cohen, A. J.; Mori-Sánchez, P.; Yang, W. Challenges for Density Functional Theory. *Chem. Rev.* **2011**, *112*, 289-320.
- (10) Cohen, A. J.; Mori-Sánchez, P.; Yang, W. Insights Into Current Limitations of Density Functional Theory. *Science.* **2008**, *321*, 792-794.
- (11) Hehre, W. J.; Ditchfield, R.; Pople, J. A. Selfconsistent Molecular Orbital Methods. XII. Further Extensions of Gaussiantype Basis Sets for Use in Molecular Orbital Studies of Organic Molecules. *J. Chem. Phys.* **1972**, *56*, 2257-2261.
- (12) Adamo, C.; Barone, V. Toward Reliable Adiabatic Connection Models Free From Adjustable Parameters. *Chem. Phys. Lett.* **1997**, *274*, 242-250.
- (13) Félix, M.; Voityuk, A. A. DFT Performance for the Hole Transfer Parameters in DNA Π Stacks. *Int. J. Quantum. Chem.* **2011**, *111*, 191-201.

- (14) Dierksen, M.; Grimme, S. The Vibronic Structure of Electronic Absorption Spectra of Large Molecules: A Time-dependent Density Functional Study on the Influence of Exact Hartree-Fock Exchange. *J. Phys. Chem. A*. **2004**, *108*, 10225-10237.
- (15) Talipov, M. R.; Boddeda, A.; Timerghazin, Q. K.; Rathore, R. Key Role of End-capping Groups in Optoelectronic Properties of Poly-p-phenylene Cation Radicals. *J. Phys. Chem. C*. **2014**, *118*, 21400-21408.
- (16) Tomasi, J.; Mennucci, B.; Cammi, R. Quantum Mechanical Continuum Solvation Models. *Chem. Rev.* **2005**, *105*, 2999-3094.
- (17) Miertuvs, S.; Scrocco, E.; Tomasi, J. Electrostatic Interaction of a Solute with a Continuum. A Direct Utilizaion of AB Initio Molecular Potentials for the Prevision of Solvent Effects. *Chem. Phys.* **1981**, *55*, 117-129.
- (18) Cossi, M.; Barone, V.; Mennucci, B.; Tomasi, J. Ab Initio Study of Ionic Solutions by a Polarizable Continuum Dielectric Model. *Chem. Phys. Lett.* **1998**, *286*, 253-260.
- (19) Cancès, E.; Mennucci, B.; Tomasi, J. A New Integral Equation Formalism for the Polarizable Continuum Model: Theoretical Background and Applications to Isotropic and Anisotropic Dielectrics. *J. Chem. Phys.* **1997**, *107*, 3032-3041.
- (20) Ribeiro, R. F.; Marenich, A. V.; Cramer, C. J.; Truhlar, D. G. Use of Solution-phase Vibrational Frequencies in Continuum Models for the Free Energy of Solvation. *J. Phys. Chem. B*. **2011**, *115*, 14556-14562.
- (21) Bauernschmitt, R.; Ahlrichs, R. Stability Analysis for Solutions of the Closed Shell Kohn--Sham Equation. *J. Chem. Phys.* **1996**, *104*, 9047-9052.
- (22) Weinhold, F.; Landis, C. R. *Valency and bonding: a natural bond orbital donor-acceptor perspective*; Cambridge University Press: 2005.
- (23) Reed, A. E.; Weinstock, R. B.; Weinhold, F. Natural Population Analysis. *J. Chem. Phys.* **1985**, *83*, 735-746.
- (24) Cossi, M.; Barone, V. Time-dependent Density Functional Theory for Molecules in Liquid Solutions. *J. Chem. Phys.* **2001**, *115*, 4708-4717.
- (25) Cammi, R.; Mennucci, B.; Tomasi, J. Fast Evaluation of Geometries and Properties of Excited Molecules in Solution: A Tamm-Dancoff Model with Application to 4-dimethylaminobenzonitrile. *J. Phys. Chem. A*. **2000**, *104*, 5631-5637.
- (26) Stratmann, R. E.; Scuseria, G. E.; Frisch, M. J. An Efficient Implementation of Time-dependent Density-functional Theory for the Calculation of Excitation Energies of Large Molecules. *J. Chem. Phys.* **1998**, *109*, 8218-8224.
- (27) Casida, M. E.; Jamorski, C.; Casida, K. C.; Salahub, D. R. Molecular Excitation Energies to High-lying Bound States From Time-dependent Density-functional Response Theory: Characterization and Correction of the Time-dependent Local Density Approximation Ionization Threshold. *J. Chem. Phys.* **1998**, *108*, 4439-4449.

(28) Bauernschmitt, R.; Ahlrichs, R. Treatment of Electronic Excitations Within the Adiabatic Approximation of Time Dependent Density Functional Theory. *Chem. Phys. Lett.* **1996**, *256*, 454-464.

(29) Wiberg, K. B.; Hadad, C. M.; LePage, T. J.; Breneman, C. M.; Frisch, M. J. Analysis of the Effect of Electron Correlation on Charge Density Distributions. *J. Phys. Chem.* **1992**, *96*, 671-679.

(30) Improta, R.; Scalmani, G.; Frisch, M. J.; Barone, V. Toward Effective and Reliable Fluorescence Energies in Solution by a New State Specific Polarizable Continuum Model Time Dependent Density Functional Theory Approach. *J. Chem. Phys.* **2007**, *127*, 074504.

(31) Improta, R.; Barone, V.; Scalmani, G.; Frisch, M. J. A State-specific Polarizable Continuum Model Time Dependent Density Functional Theory Method for Excited State Calculations in Solution. *J. Chem. Phys.* **2006**, *125*, 054103.

(32) Gierschner, J.; Cornil, J.; Egelhaaf, H. -J. Optical Bandgaps of Π -conjugated Organic Materials at the Polymer Limit: Experiment and Theory. *Adv. Mater.* **2007**, *19*, 173-191.

(33) Kuhn, H. A Quantum-Mechanical Theory of Light Absorption of Organic Dyes and Similar Compounds. *J. Chem. Phys.* **1949**, *17*, 1198-1212.

(34) Torras, J.; Casanovas, J.; Alemán, C. Reviewing Extrapolation Procedures of the Electronic Properties on the Π -conjugated Polymer Limit. *J. Phys. Chem. A.* **2012**, *116*, 7571-7583.

(35) Hückel, E. Quantentheoretische Beiträge Zum Problem Der Aromatischen Und Ungesättigten Verbindungen. III. *Z. Phys.* **1932**, *76*, 628-648.

(36) Kutzelnigg, W. What I Like About Hückel Theory. *J. Comput. Chem.* **2007**, *28*, 25-34.

(37) Talipov, M. R.; Ivanov, M. V.; Rathore, R. Inclusion of Asymptotic Dependence of Reorganization Energy in the Modified Marcus-Based Multistate Model Accurately Predicts Hole Distribution in Poly-p-phenylene Wires. *J. Phys. Chem. C.* **2016**, *120*, 6402-6408.